The Astrophysical Journal, 976:23 (16pp), 2024 November 20 https://doi.org/10.3847/1538-4357/ad7fe4

The Binary Black Hole Merger Rate Deviates from the Cosmic Star Formation Rate: A Tug of War between Metallicity and Delay Times

Adam P. Boesky[1], Floor S. Broekgaarden[1,2,3,4,5,6], and Edo Berger[1,7]
[1] Center for Astrophysics | Harvard & Smithsonian, 60 Garden St., Cambridge, MA 02138, USA
[2] Department of Astronomy & Astrophysics, University of California, San Diego, 9500 Gilman Drive, La Jolla, CA 92093, USA
[3] AstroAI, Center for Astrophysics | Harvard & Smithsonian, 60 Garden St., Cambridge, MA 02138, USA
[4] Simons Society of Fellows, Simons Foundation, New York, NY 10010, USA
[5] Department of Astronomy and Columbia Astrophysics Laboratory, Columbia University, 550 W 120th St., New York, NY 10027, USA
[6] William H. Miller III Department of Physics and Astronomy, Johns Hopkins University, Baltimore, MD 21218, USA
[7] The NSF AI Institute for Artificial Intelligence and Fundamental Interactions, USA
Received 2024 May 1; revised 2024 September 10; accepted 2024 September 24; published 2024 November 12

Abstract

Gravitational-wave detectors are now making it possible to investigate how the merger rate of binary black holes (BBHs) evolves with redshift. In this study, we examine whether the BBH merger rate of isolated binaries deviates from a scaled star formation rate density (SFRD)—a frequently used model in state-of-the-art research. To address this question, we conduct population synthesis simulations using COMPAS with a grid of stellar evolution models, calculate their cosmological merger rates, and compare them to a scaled SFRD. We find that our simulated rates deviate by factors up to 3.5 at $z \sim 0$ and 5 at $z \sim 9$ due to two main phenomena: (i) the formation efficiency of BBHs is an order of magnitude higher at low metallicities than at solar metallicity, and (ii) BBHs experience a wide range of delays (from a few megayears to many gigayears) between formation and merger. The deviations are similar when comparing to a delayed SFRD, and even larger (up to $\sim 10\times$) when comparing to SFRD-based models scaled to the local merger rate. Interestingly, our simulations find that the BBH delay time distribution is redshift dependent, increasing the complexity of the redshift distribution of mergers. We find similar results for simulated merger rates of black hole–neutron stars (BHNSs) and binary neutron stars (BNSs). We conclude that the rate of BBH, BHNS, and BNS mergers from the isolated channel can significantly deviate from a scaled SFRD, and that future measurements of the merger rate will provide insights into the formation pathways of gravitational-wave sources.

Unified Astronomy Thesaurus concepts: Compact objects (288); Binary stars (154); Gravitational waves (678)

1. Introduction

The rapidly increasing sample of gravitational-wave (GW) events detected by the Advanced LIGO and Virgo interferometers offers a new opportunity to explore the formation and properties of black holes (BHs) and neutron stars (NSs) as a function of redshift. The most recent GW catalogs (GWTC-3 and OGC-4) and independent GW data analyses already contain about 100 binary black hole (BBH) mergers out to redshifts $z \sim 1.5$ (B. P. Abbott et al. 2019; T. Venumadhav et al. 2019, 2020; B. Zackay et al. 2019; R. Abbott et al. 2021a, 2023a, 2024; S. Olsen et al. 2022; A. K. Mehta et al. 2023; A. H. Nitz et al. 2023; D. Wadekar et al. 2023), and next-generation GW detectors, such as Cosmic Explorer and the Einstein Telescope, are poised to detect stellar-mass BH mergers beyond $z \gtrsim 10$ (e.g., M. Punturo et al. 2010; D. Reitze et al. 2019; M. Maggiore et al. 2020; M. Evans et al. 2021, 2023; N. Singh et al. 2022; M. Branchesi et al. 2023; I. Gupta et al. 2023). The rate and properties of BBH, black hole–neutron star (BHNS), and binary neutron star (BNS) mergers as a function of redshift can provide invaluable insights into the physical processes underlying BH and NS formation, the massive (binary) stars that lead to their formation, their host galaxies, and the different formation channels at play (e.g., M. Fishbach et al. 2018; C. L. Rodriguez & A. Loeb 2018; S. Vitale et al. 2019; S. S. Bavera et al. 2021; K. K. Y. Ng et al. 2021; Q. Chu et al. 2022; M. Mapelli et al. 2022; L. A. C. van Son et al. 2022b; A. Ray et al. 2023; F. Santoliquido et al. 2023; M. Chruślińska 2024; A. Olejak et al. 2024; A. Vijaykumar et al. 2024). A challenge, however, is that information about the formation pathway and progenitor system is not directly imprinted in the GW observations. Inferring such properties, or making predictions for future GW detectors, therefore often requires making assumptions about the underlying merger population.

A common assumption in the literature is that the BBH (and BHNS/ BNS) merger rate, $\mathcal{R}_{\rm merge}(z)$, can be described by scaled versions of the cosmic star formation rate density (SFRD), matched to the local observed merger rate (e.g., F. Iacovelli et al. 2022; I. Gupta et al. 2023; L. Lehoucq et al. 2023). This assumption is based on the notion that GW sources are formed from massive stars, whose formation rate is described by the SFRD, which rapidly form binary compact object systems ($\sim$10 Myr; e.g., R. Kippenhahn & A. Weigert 1990) that merge after some time. There are many astrophysical processes in the evolution of binary stars, however, that can drastically alter this paradigm, leading to a merger rate that might not follow a scaled SFRD. As will be the focal point of this paper, there are two key processes within the isolated binary evolution formation channel that can cause significant deviations from the SFRD.

First, the formation efficiency of compact object binaries is metallicity dependent. The evolutionary outcome of massive (binary) stars can rely strongly on birth metallicity, as metallicity drives mass loss through stellar winds which impact, for example, the radial extension of stars and the

remnant mass of compact objects (e.g., J. S. Vink et al. 2000, 2001; N. Langer 2012). Recent work has shown that the formation yield of BBHs is strongly dependent on their birth metallicity (M. Chruslinska et al. 2018; N. Giacobbo & M. Mapelli 2018; F. S. Broekgaarden et al. 2022), resulting in a BBH merger rate that does not follow the SFRD, but an SFRD convolved with this metallicity dependence.

Second, BBH mergers may occur with a significant delay relative to the formation epoch, and the distribution of delay times can itself be metallicity dependent (e.g., K. Belczynski et al. 2016; N. Giacobbo & M. Mapelli 2018). Although massive binary stars form BBH systems (or BHNS and BNS systems) in just ∼10 Myr, the merger delay times can be as long as many gigayears (e.g., P. C. Peters 1964; C. J. Neijssel et al. 2019), resulting in a merger rate that may follow a delayed SFRD. Indeed, some GW studies model $\mathcal{R}_{\rm merge}(z)$ as a scaled SFRD combined with a delay time distribution, which is often assumed to follow a simple power law, $dn/dt \propto t^{-1}$, with a minimum delay time of ∼10–100 Myr (e.g., T. Regimbau et al. 2012; E. Belgacem et al. 2019; A. Colombo et al. 2022; F. Iacovelli et al. 2022; R. P. Naidu et al. 2022; L. Lehoucq et al. 2023; S. Borhanian & B. S. Sathyaprakash 2024).

Here, we investigate how the two aforementioned effects impact $\mathcal{R}_{\rm merge}(z)$. We employ a large set of population synthesis models for the isolated binary evolution formation pathway to simulate BBH (as well as BHNS and BNS) mergers and investigate the resulting merger rates as a function of redshift for a wide range of assumptions about stellar and binary evolution. The paper is structured as follows. We describe our models and methods in Section 2. We investigate the effects of metallicity-dependent formation yield and delay times on $\mathcal{R}_{\rm merge}(z)$ in Sections 3.1 and 3.2, respectively. In Section 3.3, we assess the accuracy of models from the literature by comparing our simulated rates to SFRD-based models scaled to the inferred local BBH merger rate and convolved with different delay time distributions. We discuss our results for BHNS and BNS mergers in Section 3.4. We end with a discussion in Section 4 and a summary of our key findings in Section 5.

2. Methods

2.1. Population Synthesis Simulated Merger Rates

We use the simulation output and methodology from A. Boesky et al. (2024), which are briefly summarized here. A. Boesky et al. (2024) present a population of simulated compact object mergers formed through the isolated binary evolution pathway. The simulations are generated using Compact Object Mergers: Population Astrophysics and Statistics (COMPAS;[8] Team COMPAS et al. 2022), a rapid population synthesis code. COMPAS simulates the evolution of massive stars based on analytical fitting formulae for single and binary star evolution by J. R. Hurley et al. (2000, 2002), derived from stellar evolution tracks presented in O. R. Pols et al. (1998), as well as earlier work by P. P. Eggleton et al. (1989) and C. A. Tout et al. (1996).

A. Boesky et al. (2024) study two two-parameter-varied grids of simulations. Here, we only focus on the grid that varies the common-envelope (CE) efficiency, $\alpha_{\rm CE}$, and mass transfer efficiency, β, parameters. The CE phase results from dynamically unstable mass transfer in which the companion star is engulfed in the donor's envelope and tightens the binary through drag (see N. Ivanova et al. 2020, and the references therein). COMPAS employs the "$\alpha_{\rm CE} - \lambda$" formalism (R. F. Webbink 1984; M. de Kool 1990) to parameterize the CE phase. The $\alpha_{\rm CE}$ parameter is of particular interest when investigating the merger rate because it is capable of significantly reducing the binary separation, and thus potentially altering the expected $dn/dt \propto t^{-1}$ delay time distribution (e.g., K. Belczynski et al. 2018; A. Vigna-Gomez et al. 2018). Our grid uses four CE efficiency values, $\alpha_{\rm CE} = 0.1$, 0.5, 2, and 10, which comprise a range representative of prior studies (e.g., A. Vigna-Gomez et al. 2018; S. S. Bavera et al. 2021; F. Santoliquido et al. 2021; F. S. Broekgaarden et al. 2022; A. Dorozsmai & S. Toonen 2024). In tandem with $\alpha_{\rm CE}$, we also vary the accretion efficiency $\beta = \Delta M_{\rm acc}/M_{\rm donor}$, where $\Delta M_{\rm donor}$ and $\Delta M_{\rm acc}$ are the changes in the mass of the donor and accretor stars, respectively. We use $\beta = 0.25$, 0.5, and 0.75 to reflect the parameter's theoretical range of [0, 1] (see earlier works; F. S. Broekgaarden et al. 2022; L. A. C. van Son et al. 2022b; A. Dorozsmai & S. Toonen 2024). Henceforth, we refer to the model with $\alpha_{\rm CE} = 2$ and $\beta = 0.5$ as the "fiducial" model.

Throughout our study, we adopt a popular model of the SFRD from P. Madau & M. Dickinson (2014, Equation (15)):

$$\psi(z) = a\frac{(1+z)^b}{1+[(1+z)/c]^d}\, M_\odot\ {\rm yr}^{-1}\,{\rm Mpc}^{-3}, \tag{1}$$

with $a = 0.01$, $b = 2.6$, $c = 3.2$, and $d = 6.2$ (P. Madau & T. Fragos 2017). The true SFRD is uncertain, and exploring the impact of the assumed SFRD model is left for future research. We expect the qualitative results in this work, however, to be robust under different choices for the SFRD.

To calculate the merger rate of a simulated binary population of BBH, BHNS, or BNS mergers, we convolve a metallicity-specific SFRD, $\mathcal{S}(Z_i, z)$, with the formation rate of the population:

$$\begin{aligned}\mathcal{R}_{\rm merge}(t_m, M_1, M_1) &\equiv \frac{d^4N_{\rm merge}}{dt_m dV_c dM_1 dM_2}(t_{\rm m}, M_1, M_2)\\ &= \int dZ_i \int_0^{t_m} dt_{\rm delay}\,\mathcal{S}(Z_i, z(t_{\rm form} = t_m - t_{\rm delay}))\\ &\times \frac{d^4N_{\rm form}}{dM_{\rm SFR}\,dt_{\rm delay}\,dM_1 dM_2}(Z_i, t_{\rm delay}, M_1, M_2),\end{aligned} \tag{2}$$

where t_m is the time of the merger in the comoving frame, $t_{\rm delay}$ is the time between the formation and merger of a binary, and M_1 and M_2 are the binary component masses. To obtain the metallicity-dependent star formation rate $\mathcal{S}(Z_i, z(t_{\rm form}))$, we convolve the commonly used galaxy stellar mass function from B. Panter et al. (2004) with the mass–metallicity relation from X. Ma et al. (2016), and multiply the result with the SFRD in Equation (1) (e.g., C. J. Neijssel et al. 2019; F. S. Broekgaarden et al. 2022). We use `astropy` to transform t_m to a redshift using the Wilkinson Microwave Anisotropy Probe 9 cosmology.[9] For more details on the merger rate and its calculation, see the methodology in Team COMPAS et al. (2022).

[8] https://compas.science

[9] We find that the rates are not significantly impacted by the choice of cosmology (e.g., C. J. Neijssel et al. 2019).

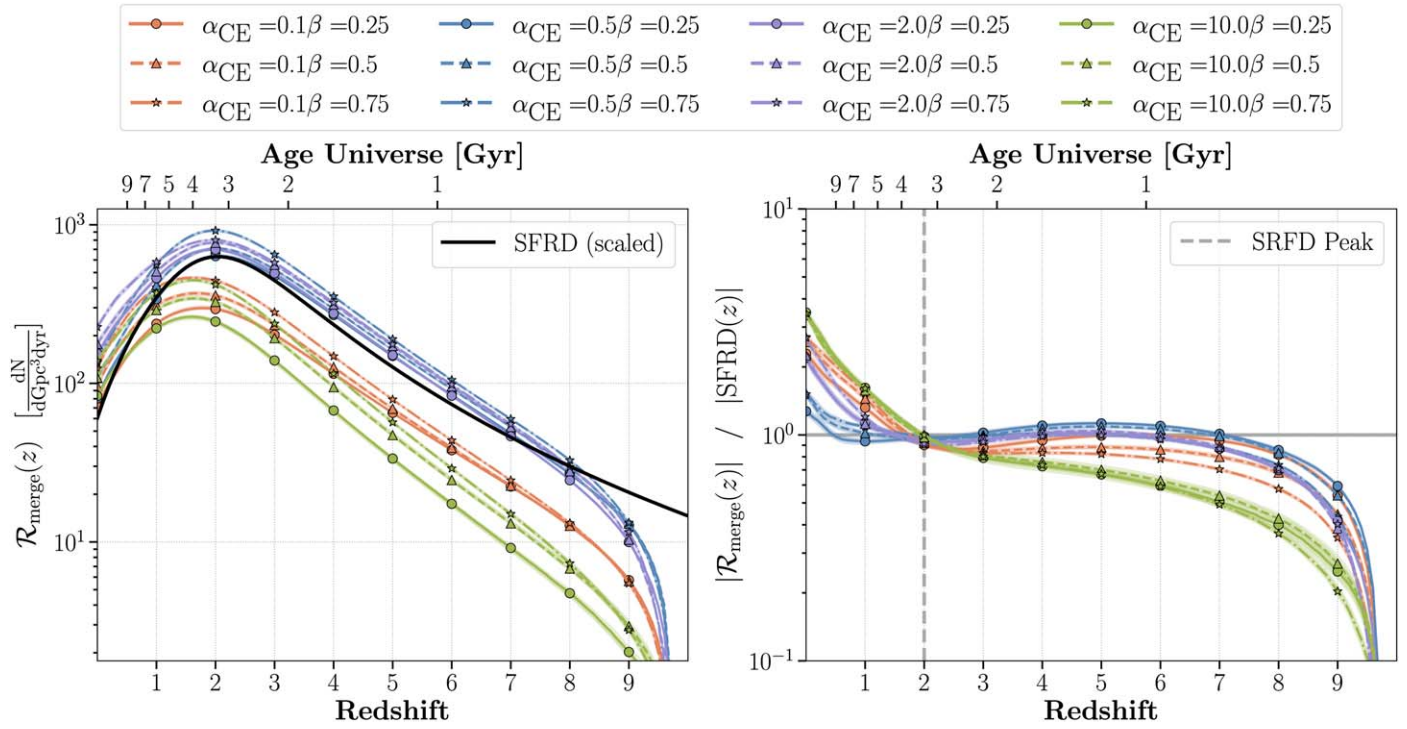

Figure 1. Left: the BBH merger rate as a function of redshift for the α_{CE} and β model variations explored in this paper compared to the SFRD scaled arbitrarily (black line). Right: the BBH merger rate divided by the SFRD, where we normalize the areas of both to one. The horizontal gray line indicates a merger rate that follows the SFRD, and the dashed vertical gray line is the redshift of the SFRD peak. In both panels we include the 1σ and 2σ confidence intervals calculated by bootstrapping the simulation results to show the sampling uncertainty (note that the uncertainties are typically the same size as the width of the lines). The sharp decline in the merger rate at $z \sim 9$ is due to star formation starting at $z = 10$ in our calculations and the fact that mergers are delayed.

2.2. Star Formation Rate Density–based Toy Model Merger Rates

To investigate whether popular, simplistic models of the merger rate are representative of population synthesis results, we compare our simulations to three models from the literature. Throughout this study, we will refer to these as "toy models." The first, and simplest, toy model is a scaled SFRD. The second is a scaled SFRD convolved with a constant delay time of $t_{delay} = 20$ Myr. The third is an SFRD convolved with a $dn/dt \propto 1/t$ delay time distribution that has a minimum delay time of ~20 Myr (similar to studies including T. Regimbau et al. 2012; A. Colombo et al. 2022; F. Iacovelli et al. 2022; L. Lehoucq et al. 2023; S. Borhanian & B. S. Sathyaprakash 2024).

For all toy models, we use the SFRD described in Equation (1) to match the SFRD assumed for calculating the merger rate. Throughout this paper, we compare toy models to our population synthesis simulated merger rates (Equation (2)) by normalizing both such that their areas integrate to unity, and then dividing the simulated $\mathcal{R}_{merge}(z)$ by the toy model. We first discuss results for the scaled SFRD toy model, and then we describe results for the two delayed SFRD toy models in Section 3.3 and beyond.

3. Results: Deviation from the Star Formation Rate Density

In Figure 1, we show the BBH merger rates produced with our suite of models, and compare them to an arbitrarily scaled SFRD. In the left panel, we find that our simulated models produce different merger rate distributions as a function of redshift, and also lead to different merger rate magnitudes. Models with $\alpha_{CE} = 0.5$ and 2.0 produce merger rates of factors ~3–10 higher than models with $\alpha_{CE} = 0.1$ and 10.0. This is a result of $\alpha_{CE} = 0.1$ causing binaries to merge before the stars are able to become BBHs, while $\alpha_{CE} = 10$ does not tighten the binaries enough to merge within a Hubble time.[10]

Most importantly for the scope of this study, we find that the redshift evolution of our simulated merger rates deviates from the scaled SFRD toy model. These deviations from the SFRD are highlighted in the right panel of Figure 1, in which we normalize the merger rates and divide them by the normalized SFRD.[11] We find that the normalized BBH merger rates tend to be higher (up to a factor of 3.5) compared to the SFRD at low redshift $z \lesssim 1.5$, as is visible by all lines exceeding unity. The merger rates approach the scaled SFRD around redshift 2, and then fall below the SFRD above redshifts $\gtrsim 2$, with the exact z at which this occurs depending on the model. Some models only fall below the SFRD line at high redshifts $z \gtrsim 7$, such as those with $\alpha_{CE} = 0.5$. We find deviations of our simulated merger rates from the SFRD as high as factors of 5 (for the $\alpha_{CE} = 10$ models around $z \sim 9$). The first three columns in Table 1 in the Appendix provide statistics on the relative ratios between the (normalized) simulated BBH merger rates and SFRD from $z = 0$ to $z = 9$. A. Boesky et al. (2024) quantify the shape of each model's merger rate using the differential, and shows how the merger rate differentials compare to that of the assumed SFRD (see their Figure 3).

Despite model-to-model variations, the general trend among our simulated merger rates in Figure 1 indicates shared

[10] We elaborate on this "sweet spot" of α_{CE} in Section 3.2.

[11] We note that this normalization is chosen to investigate the *relative* differences between our simulations and the SFRD toy model, but leads in practice to minimal differences around the merger rate peak $z \sim 2$. See Section 3.3 for results that scale by the local merger rate instead.

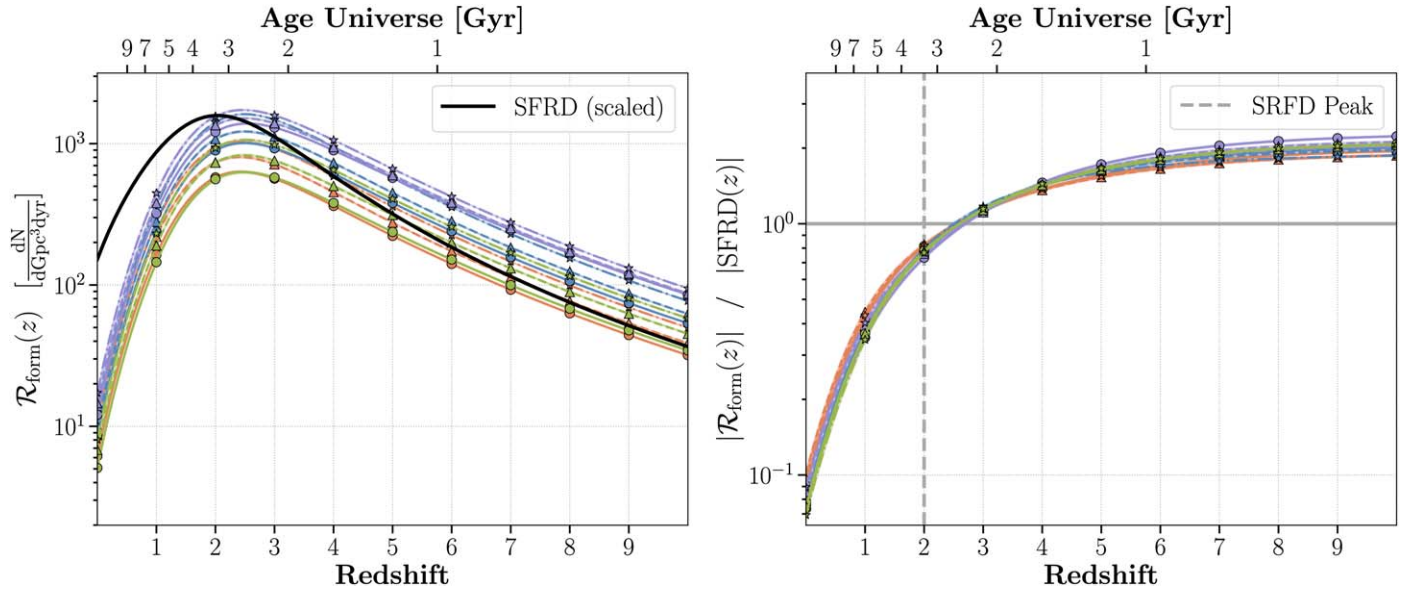

Figure 2. Same as Figure 1, but for the BBH formation rate (formation is defined as the moment when the second BH forms). The peak of the BBH formation rate is clearly shifted to higher redshifts than the SFRD due to a higher BBH formation efficiency at lower metallicities.

underlying physical processes that cause $\mathcal{R}_{\rm merge}(z)$ to deviate from the SFRD. As stated in Section 1, the physical sources of merger rate–SFRD deviations is the effect of metallicity and delay times, which we explore comprehensively in the following two sections.

3.1. The Effect of Metallicity on the Merger Rate

First, we focus on the effect of the metallicity-dependent formation efficiency on $\mathcal{R}_{\rm merge}(z)$ for BBHs. In the left panel of Figure 2, we plot the BBH formation rate as a function of redshift, $\mathcal{R}_{\rm form}(z)$ (Equation (1) in F. S. Broekgaarden et al. 2021), for all our models and in the right panel of Figure 2, we plot the ratio of the BBH formation rate relative to the scaled SFRD (the toy model). If the formation yields of BBHs were independent of metallicity, the formation rate of BBHs as a function of redshift would exactly follow the SFRD since the simulations assume all other initial conditions (e.g., initial mass and initial separation) to be independent of the initial metallicity, and the time required for massive stars to form BBHs is negligible on this scale. We find the following results.

First, we observe that, similarly to $\mathcal{R}_{\rm merge}(z)$ in Figure 1, models with $\alpha_{\rm CE} = 0.5$ and 2.0 tend have higher $\mathcal{R}_{\rm form}(z)$ than the other two $\alpha_{\rm CE}$ values by a factor of up to $\sim$5. Notably, there is very little variation in the redshift evolution of $\mathcal{R}_{\rm form}(z)$ between models, and they all deviate from the scaled SFRD—the peak of the BBH formation rate from all models is at a higher redshift ($z \approx 2.5$) than the peak of the SFRD at $z = 2$. As a result, we find that the BBH formation rate in the simulated $\mathcal{R}_{\rm form}(z)$ is suppressed at $z \lesssim z_{\rm peak}$ compared to the scaled SFRD with deviations of up to an order of magnitude at $z \sim 0$. The simulated BBH rate is relatively boosted for $z \gtrsim z_{\rm peak}$ by a factor of $\sim$2 compared to the SFRD. All in all, our results find a metallicity dependence in the formation rates of population synthesis simulations which favors high-z BBH formation, thus favoring the rate of merging BBHs at higher redshifts compared to lower redshifts.

To further probe the metallicity dependence of BBH formation, we show the simulated formation rates of BBHs as a function of initial metallicity, Z_i, in the top panel of Figure 3. We find that as Z_i increases, the BBH formation yield falls off more and more rapidly, as much as an order of magnitude by $Z_\odot/2$, and 3 orders of magnitude by 2 $Z_\odot$. This rapid decline is consistent with findings for BBH mergers formed from isolated binary evolution in recent literature (e.g., M. Chruslinska et al. 2018; N. Giacobbo & M. Mapelli 2018; N. Giacobbo et al. 2018; J. Klencki et al. 2018; C. J. Neijssel et al. 2019; F. Santoliquido et al. 2021; F. S. Broekgaarden et al. 2022; A. Dorozsmai & S. Toonen 2024). Since the mean metallicity increases with cosmic time, higher BBH formation efficiency at low progenitor metallicity results in a higher BBH formation rate relative to the SFRD at higher redshifts ($z \gtrsim 2.5$, as is visible in Figure 2). The redshift at which we observe notable increases in the formation rate is around where the proportion of formed stars has a considerable change in birth metallicity based on the Madau–Dickinson prescription (see Appendix B for details on the metallicity-dependent SFRD). Low model-to-model variation in the relationship between metallicity and formation yield leads to the tight spread (within a factor of few) of the BBH formation rates among the models that we observe in Figure 2 (e.g., M. Chruslinska et al. 2018; F. Santoliquido et al. 2021; F. S. Broekgaarden et al. 2022). Boosted BBH formation efficiency at low birth metallicity is predominantly caused by less wind loss through line-driven stellar winds at low metallicity, which leads to tighter binary systems (e.g., because more mass needs to be expelled during a CE event) and fewer systems that disrupt during supernova. We discuss this in more detail in Appendix A.

3.2. The Effect of the Delay Time on the Merger Rate

The delay times ($t_{\rm delay}$) between the formation and merger of BBHs, can range from a few megayears to greater than the Hubble time (K. Belczynski et al. 2016; N. Mennekens & D. Vanbeveren 2016; V. M. Lipunov et al. 2017; S. Stevenson et al. 2017; J. J. Eldridge et al. 2019) and lead the BBH merger rate to peak at a lower redshift than the formation rate. It is generally thought that the delay time distribution roughly

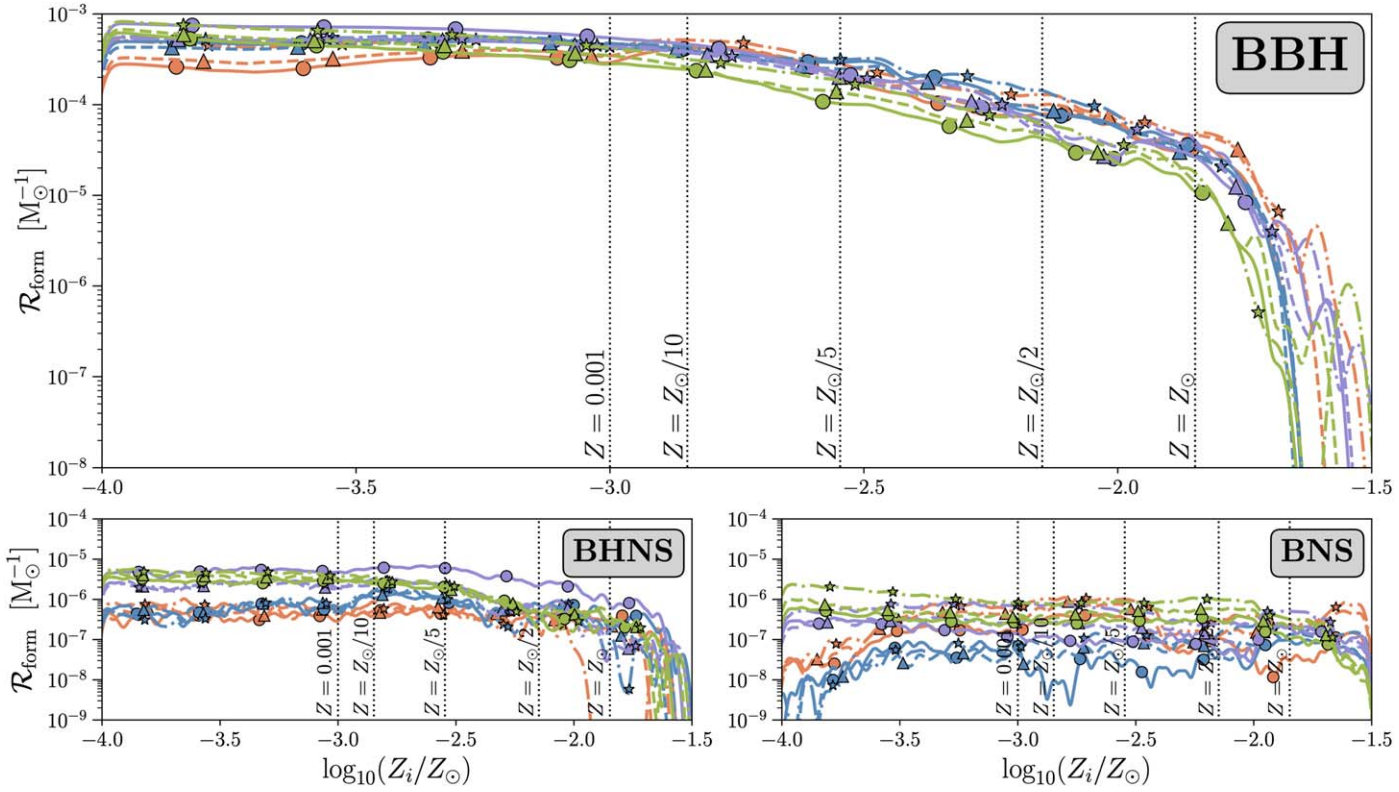

Figure 3. The formation yield of BBHs, BHNSs, and BNSs that will merge within a Hubble time, per solar mass of star formation, $d\mathcal{R}_{\rm form}/dM_{\rm SFRD}$, as a function of birth metallicity, Z_i, for all models. We choose initial metallicities for each binary by sampling randomly from a log-uniform metallicity distribution from $Z_i = 0.0001$ to $Z_i = 0.03$. We then obtain $\mathcal{R}_{\rm form}(Z_i)$ using a kernel density estimation over the initial metallicities of the simulated binaries. The decline in BBH formation efficiency at $Z_i \gtrsim Z_\odot/5$ is clearly visible.

follows $dn/dt \propto t^{-1}$ with a minimum delay time, $t_{\rm min}$, typically bound between 10 and 500 Myr (e.g., T. Regimbau et al. 2012; A. Colombo et al. 2022; F. Iacovelli et al. 2022; R. P. Naidu et al. 2022; S. Borhanian & B. S. Sathyaprakash 2024).

To understand the effect of the delay times, we first investigate whether the BBH delay times are dependent on the formation redshift. In the left panel of Figure 4, we show the normalized distributions of the delay times for binaries formed at $z = 0.2$, 2, and 6 for our fiducial model. We do indeed find redshift dependence, as the distributions for $z = 0.2$ and $z = 2$ have flatter slopes than $1/t$—specifically, the best fits are $t^{-0.63 \pm 0.016}$, $t^{-0.77 \pm 0.007}$, and $t^{-0.95 \pm 0.003}$ for $z = 0.2$, 2.0, and 6.0, respectively, in the region $t_{\rm delay} > 100$ Myr. We also find that the delay time distributions at all three redshifts flatten out for delay times $\lesssim$500 Myr (compared to $t_{\rm delay} > 500$ Myr).

In the right panel of Figure 4 we show the distributions of delay times from our fiducial model, differentiating observable and unobservable mergers, where the latter are those formed at a given redshift with delay times longer than the time between their formation and a Hubble time. We find that the majority of binaries formed at $z = 0.2$ merge after $z = 0$. Furthermore, while there are around an order of magnitude more BBH mergers at $z = 2.0$ than to $z = 6.0$, the proportion of observable mergers at $z = 2$ is less than that from $z = 6.0$ due to differences in the range of delay times that lead to mergers we can detect.

In Figure 5, we show how the median delay time for BBHs merging in a Hubble time evolves with redshift for all models. We find two main results. First, the median delay time evolves differently as a function of redshift for the different models. Among our simulations there are four sets of models with similar median $t_{\rm delay}$ behavior throughout redshift, which can be differentiated by the $\alpha_{\rm CE}$ value. This suggests that the CE mass transfer phase and the CE efficiency parameter used in the simulations are important in determining a binary's delay time (e.g., Q. Chu et al. 2022) and that the effect of $\alpha_{\rm CE}$ on the delay time distribution is redshift dependent. We find that the median delay time in Figure 5 does not increase monotonically with the $\alpha_{\rm CE}$ value. This is due to the relationship between $\alpha_{\rm CE}$ and the post-CE separation: smaller $\alpha_{\rm CE}$ values require the binary's orbit to shrink more for successful envelope ejection, which in turn leads to significantly shorter delay times (P. C. Peters 1964). There is, however, a sweet spot for the $\alpha_{\rm CE}$ value: values that are too low prevent the CE from being successfully ejected, and the system instead undergoes a stellar merger, leading to the nonmonotonic behavior (e.g., M. U. Kruckow et al. 2018; S. S. Bavera et al. 2021; F. S. Broekgaarden et al. 2022). Second, the delay time medians are not constant throughout cosmic history, as can be seen by the decrease in the median BBH delay time as a function of redshift for nearly all models in Figure 5. This is because at higher redshifts, stars form with lower metallicities so experience weaker stellar winds and less radial expansion. These conditions typically lead binary systems to retain more mass, experience less orbital widening, and undergo the same evolutionary pathway in a tighter orbit. Combined, this causes binaries to form BBH systems with shorter orbits at lower metallicity, which reduces the typical simulated BBH delay time at higher redshifts. The models with $\alpha_{\rm CE} = 2.0$ have the most distinct median delay time z evolution; this unique redshift dependence is caused by a drastic increase in the proportion of mergers formed through the classic CE channel at higher redshift that leads to shorter delay times compared to the

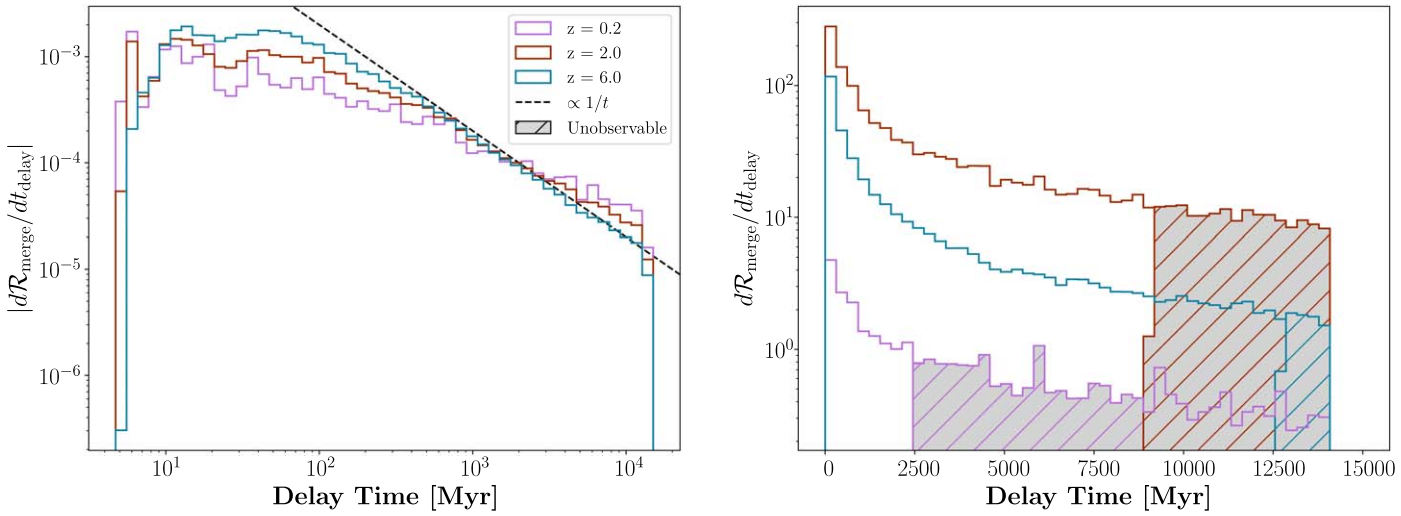

Figure 4. The BBH delay time distributions from our fiducial model for binaries formed at redshifts 0.2, 2, and 6. (Left) The distributions normalized to an area of one. The bin widths are log-uniformly and uniformly spaced in the left and right panels, respectively. (Right) The three gray hatched regions are the portion of each distribution that would not merge by $z = 0$. The lowest $t_{\rm delay}$ bins (those with $t_{\rm delay} \lesssim 10$ Myr) suffer from sampling uncertainty.

"only stable mass transfer channel" for these simulations (in agreement with, e.g., A. Olejak et al. 2022; L. A. C. van Son et al. 2022a). See Appendix D for more details on the formation channel breakdown of our simulations throughout cosmic history.

3.3. Comparison to Delayed Star Formation Rate Density Models and Models Scaled to the Local Merger Rate

So far, we have presented the deviations of population synthesis simulated BBH merger rates from a scaled SFRD, but we now consider whether our simulated merger rates deviate from a delayed SFRD. This is motivated by—in addition to the support for and use of delays in models from the literature—our findings in Section 3.2 that the delay time distribution of BBH mergers can be complex and variable between models. We use two different delayed SFRD models: (i) a scaled SFRD convolved with a delay time distribution $dn/dt \propto \delta(t - c)$, where $c = 20$ Myr, and (ii) a scaled SFRD convolved with a delay time distribution $dn/dt \propto 1/t$ with a minimum delay time of 20 Myr. See Section 2.2 for more details and references on the delayed toy models.

The top panels in Figure 6 show the deviations of our simulated $\mathcal{R}_{\rm merge}(z)$ from the SFRD model with constant $t_{\rm delay}$. We find that at high redshifts ($z \gtrsim 5$), the population synthesis merger rates deviate by factors up to $\sim$3 from the constant delay toy model—this is slightly less, 2% versus 4% at $z = 6$ and 1% versus 13% at $z = 7$, than the deviations from the SFRD model with no delays (see Table 1). On the other hand, at low redshifts, particularly for $z \sim 0$, the deviations are up to a factor of 5, which is larger than deviations without delay times (which has deviations up to 3× at $z \sim 0$).

In the bottom panels of Figure 6 we show the deviations of our simulated BBH merger rates from an SFRD with a $1/t$ delay time distribution. This toy model peaks at a lower redshift of $z \sim 1.5$ compared to $z = 2$ for the nondelayed or constant delayed SFRD merger rate models. We find that our population synthesis model merger rates deviate with factors up to 5 at low redshifts $z \lesssim 2$ from the $1/t$ delayed SFRD merger rate model and up to factors of 3 at high redshift $z \sim 9$ (see Table 1). Finally, it is important to note that there is a considerable difference between the effect of convolving the SFRD with a $1/t$ versus constant delayed distribution; therefore, it is crucial that the high $t_{\rm delay}$ tail is considered by studies in the future.

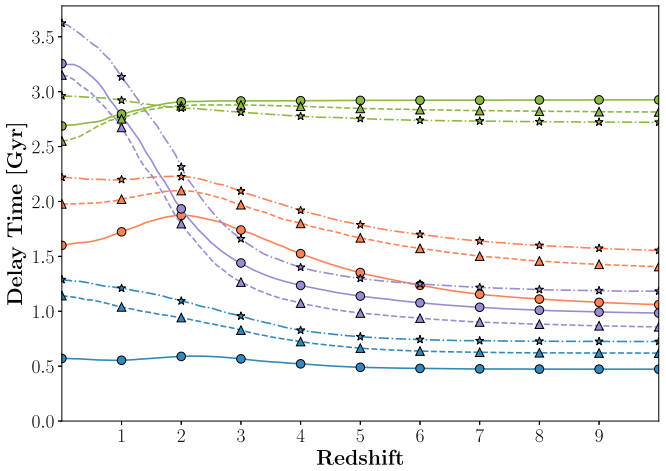

Figure 5. The median delay times of BBH mergers for each model in grid A as a function of redshift. The median only includes BBHs that merge in a Hubble time for each redshift.

Lastly, in Figure 7 we show the deviations of our simulated merger rates from the toy models where we compare by scaling to the local merger rate $\mathcal{R}_0 \equiv \mathcal{R}_{\rm merge}(0)$—a scaling often chosen for SFRD-based merger rate models in the literature (e.g., E. Belgacem et al. 2019; A. Colombo et al. 2022; F. Iacovelli et al. 2022; L. Lehoucq et al. 2023; S. Borhanian & B. S. Sathyaprakash 2024). Interestingly, we find that the population synthesis simulated merger rates deviate by factors up to 20 compared to each of the SFRD models, with the most significant deviations occurring in the range of redshifts $z \gtrsim 3$. These deviations are significantly larger compared to those experienced when we scaled the rates by area. Hence, using phenomenological models for the BBH merger rate that scale the SFRD by the local merger rate can lead to the largest deviations from the simulated population synthesis merger rates, especially for $z \gtrsim 3$.

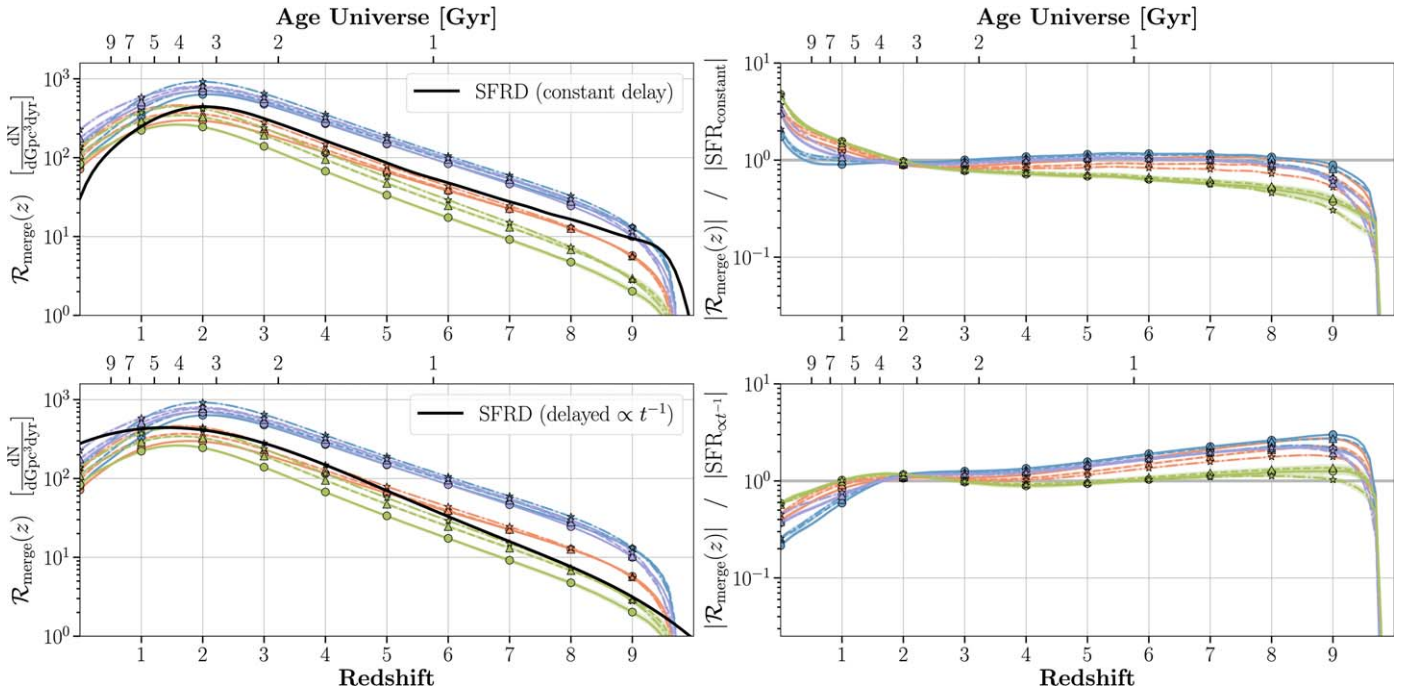

Figure 6. BBH merger rate as a function of redshift compared to toy models assuming a scaled SFRD with a constant delay time of 20 Myr (top row) and a delay time distribution of $dn/dt \propto 1/t$ with a minimum delay time of 20 Myr (bottom row). Labels and colors are the same as in Figure 1.

3.4. The Black Hole–Neutron Star and Binary Neutron Star Merger Rates

In Figures 8 and 9, we investigate the merger rate for BHNSs and BNSs, respectively. For both the BHNS and BNS mergerrates, deviations from the SFRD are generally similar to those of the BBH merger rate—most of our simulations have a proportionally higher rate of mergers than stars formed at low redshift ($z \lesssim 2$), and a lower rate at high redshift ($z \gtrsim 4$), which are caused by our choice of scaling and the fact that the merger rates peak at lower redshift compared to the SFRD. There are, however, considerably more model-to-model variations for the BNS and BHNS merger rates than the BBH merger rate. This stems from the fact that the formation efficiency–metallicity relationship has a markedly greater influence on BHNS and BNS mergers—differing by as much as 2 to 3 orders of magnitude—compared to BBH mergers, which vary within an order of magnitude, as can be found in Figure 3. These findings are consistent with similar outcomes reported in the literature (M. Chruslinska et al. 2018; N. Giacobbo & M. Mapelli 2018; J. Klencki et al. 2018; C. J. Neijssel et al. 2019; J. Román-Garza et al. 2021; F. S. Broekgaarden et al. 2022). In our simulations, BHNS and BNS mergers are more commonly formed by binaries that experience a CE phase than BBHs, leading the BHNS and BNS simulations to be particularly sensitive to the value of $\alpha_{\rm CE}$.

Interestingly, we find that many of the BHNS and BNS merger rates in Figures 8 and 9 demonstrate significantly different behavior from the BBH rates and SFRD-based toy models. For example, most of the BHNS merger rates have a significantly steeper drop-off after the merger rate peak in Figure 8. In addition, some of the BNS models in Figure 9 show evidence of an additional break in the merger rate slope before the peak, such as the model with $\alpha_{\rm CE} = 0.1$ and $\beta = 0.25$ around $z = 0.5$. This phenomenon is due to the complex convolution of the SFRD, formation efficiency of BHNSs and BNSs, and delay time distributions, and it lends weight to considering merger rates that deviate from an SFRD-like rate in future studies (e.g., E. Payne & E. Thrane 2023; T. A. Callister & W. M. Farr 2024).

4. Discussion

4.1. Other Formation Channels

This study has investigated the redshift evolution of the merger rate of BBHs (and BNSs and BHNSs) formed by the isolated binary evolution channel. Formation pathways beyond the isolated binary evolution channel, however, can contribute and impact the BBH merger rate as a function of redshift beyond the effects discussed in this paper (e.g., M. Zevin et al. 2021; G. Franciolini et al. 2022; I. Mandel & F. S. Broekgaarden 2022; A. Q. Cheng et al. 2023).[12] Studying their effects in detail is beyond the scope of this paper, but we discuss the dominant redshift behavior of these formation channels below.

BBHs formed from Population III stars (i.e., extremely metal-poor stars) are thought to merge at a significantly different rate than the isolated binary evolution channel: they begin merging at redshifts as early as $z \sim 20$ and peak around $z \sim 10$ (K. Belczynski et al. 2017; T. Kinugawa et al. 2020; K. Hijikawa et al. 2021; B. Liu & V. Bromm 2021; F. Santoliquido et al. 2023). The redshift evolution of Population III mergers is still debated and depends strongly on the assumed binary formation and interaction mechanisms that can bring BHs close together (e.g., T. Kinugawa et al. 2014, 2020; K. Belczynski et al. 2017; B. Liu & V. Bromm 2021)

The merger rate for BBHs formed in dense star clusters is also still under debate and is heavily influenced by simulation

[12] The evidence for multiple formation channels from observations is still under debate. Recent studies (e.g., M. Fishbach et al. 2022; J. Godfrey et al. 2023) find evidence for substantial contributions from the isolated binary evolution channel of BBHs, but large uncertainties remain (e.g., G. Franciolini et al. 2022; H. Tong et al. 2022).

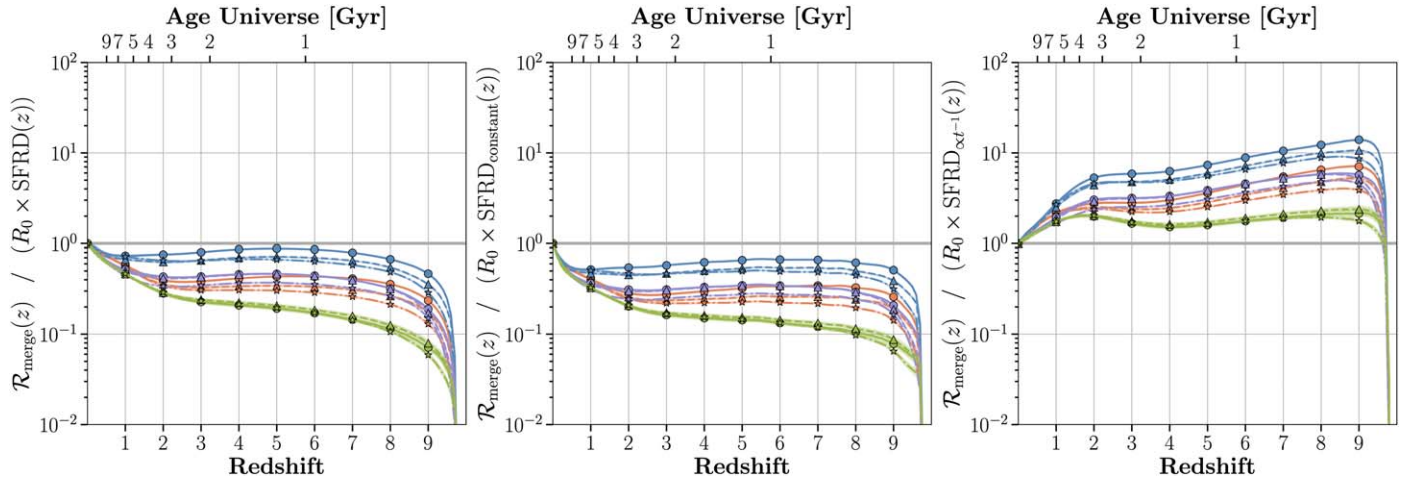

Figure 7. BBH merger rate as a function of redshift compared to toy model merger rates assuming a scaled SFRD (left), a scaled SFRD with constant delay times (middle), and a scaled SFRD with a t^{-1} delay time distribution (right). All simulations are normalized to the same intrinsic merger rate $R_{\rm merge,0}$. We assumed minimum delay times for the middle and right panel of 20 Myr. Labels and colors are the same as in Figure 1.

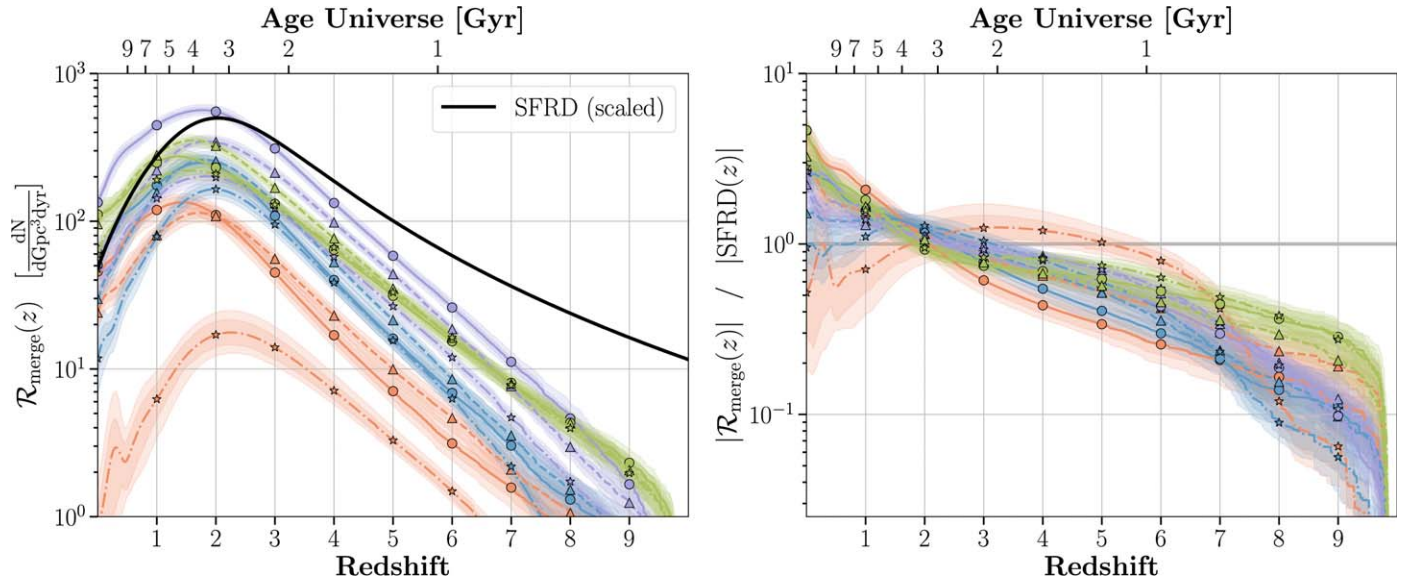

Figure 8. Same as Figure 1 but for BHNS mergers.

assumptions and host cluster properties (see N. Choksi et al. 2019, and the references therein). Some studies find that the globular cluster BBH merger rate gradually increases at small redshifts until a peak around $z \sim 2$–3 and a sharp drop-off beyond $z \gtrsim 4$ (see C. L. Rodriguez & A. Loeb 2018; N. Choksi et al. 2019). K. Kritos et al. (2024) and M. Mapelli et al. (2022) found something similar, but with a longer high-redshift tail, as they assume higher cluster formation rates at high z. Other studies instead find a monotonically increasing function of redshift starting from $z \sim 0$ out to their assumed starting epoch for a single burst of globular cluster formation around $z \sim 3$–4, leading to a merger rate that peaks around $z \sim 3$–4 and then drops immediately to zero (C. L. Rodriguez et al. 2016; G. Fragione & B. Kocsis 2018). The sharp decrease in merger rate beyond $z \gtrsim 4$ seen in most simulations is because clusters have not had sufficient time to undergo core collapse, a process during which BHs sink to the center of clusters and undergo the many dynamical interactions that dominate BBH merger production. Finally, C. S. Ye & M. Fishbach (2024) recently found that the redshift distribution of the BBH merger rate from globular clusters is correlated with primary mass, and that the peak of the merger rate is at higher z for binaries with primary mass > 30 $M_\odot$, and even higher z for primary mass > 40 $M_\odot$.

The merger rate of BBHs formed from chemically homogeneous evolution is still under debate and could either lead to a peak earlier or later than isolated binary evolution, mostly depending on the binary interaction and initial conditions assumed in the simulation (for more details see S. E. de Mink & I. Mandel 2016; I. Mandel & S. E. de Mink 2016; L. du Buisson et al. 2020; J. Riley et al. 2021).

BBHs formed from primordial origins can merge as early as $z \sim 1000$ and are thought to follow a redshift rate that increases monotonically with increasing redshift as $\mathcal{R}_{\rm merge} \propto t(z)^{-34/37}$ (e.g., M. Raidal et al. 2019; V. De Luca et al. 2020, 2021; G. Franciolini et al. 2022).

It will be important for future studies to further explore differences between the BBH merger rates from different

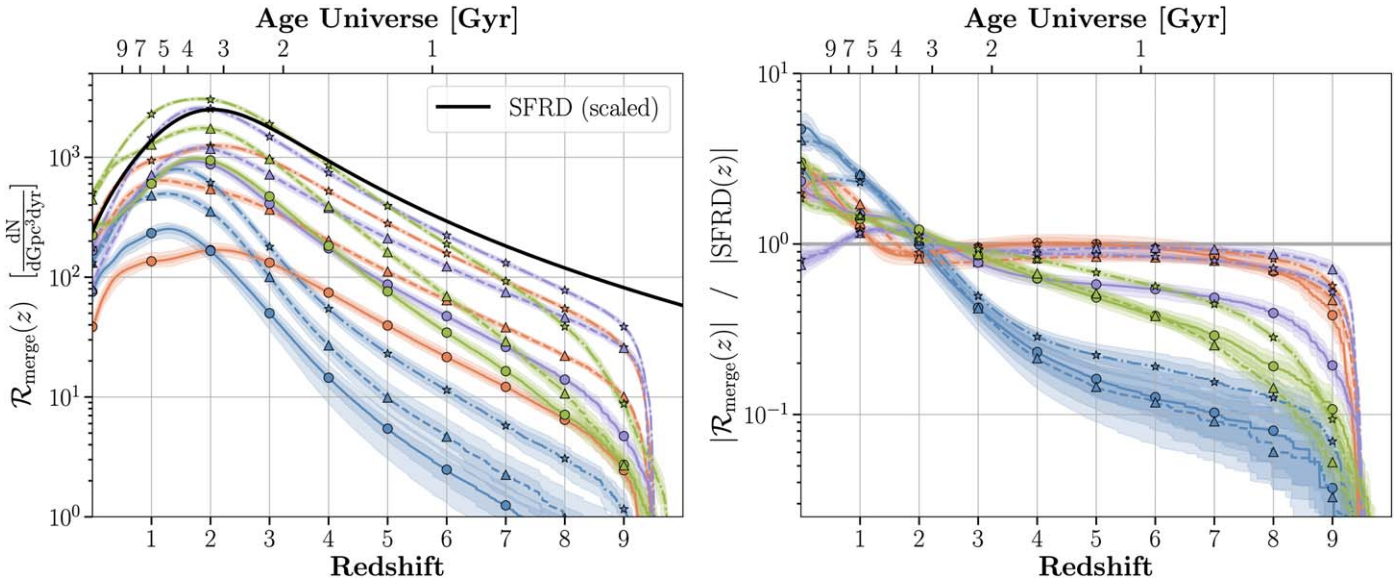

Figure 9. Same as Figure 1 but for BNS mergers.

formation pathways (e.g., M. A. S. Martinez et al. 2020; M. Zevin et al. 2021; S. S. Bavera et al. 2022b; M. Mapelli et al. 2022).

4.2. Observing the Merger Rate

It is challenging to infer the merger rate as a function of redshift from observations. The local BHNS, BNS, and BBH merger rates have been constrained using GWs, pulsars, and BNSs (and the lack of BH–pulsar binaries), as well as short gamma-ray bursts (sGRBs; and their host galaxies) and *r*-process enrichment arguments; nevertheless, large uncertainties in these methods remain (see I. Mandel & F. S. Broekgaarden 2022, and the references therein). Observations of the rate as a function of redshift remain scarce. The authors of the latest GWTC-3 catalog population inference study found that the rate in the range $0 \lesssim z \lesssim 1.5$ increases proportionally to $(1+z)^{\kappa}$ with $\kappa = 2.9^{+1.7}_{-1.8}$ (R. Abbott et al. 2023b). This value of κ is similar to the slope of the SFRD, indicating that the BBH redshift rate follows the SFRD at low redshift (which was also confirmed by B. Edelman et al. 2023; A. H. Nitz et al. 2023), though large uncertainties remain due to the limited sample of GW observations and the lack of models considered (e.g., the analysis from R. Abbott et al. 2023b assumed that the BBH mass distribution does not change as a function of redshift). Other studies using different models to analyze the GW data found evidence that the slope of the BBH merger rate might deviate from that of the SFRD (E. Payne & E. Thrane 2023; T. A. Callister & W. M. Farr 2024). We leave direct comparison to observations for future studies, and refer the reader to the discussion in A. Ray et al. (2023) for more on this topic.

Besides BBHs, the merger rates of BHNS and BNS systems as a function of redshift will also be constrained by future observing runs and next-generation detectors. The merger rate of BNSs (and potentially BHNSs) can also be constrained from electromagnetic observations of GRBs (see, e.g., E. Berger 2014; W. Fong et al. 2015; A. E. Nugent et al. 2022; M. Zevin et al. 2022, and the references therein)—although, in practice, this will require a large sample of sGRB with associated host galaxies as well as a better understanding of sGRB jet physics.

In coming years, new observing runs, including O4 and O5, are poised to increase the number of BBH merger detections to ~500 out to $z \sim 2$, which will help constrain the BBH merger rate as a function of redshift (B. P. Abbott et al. 2018).[13] Moreover, next-generation GW detectors, such as the Cosmic Explorer and Einstein Telescope, are expected to detect stellar-mass BH mergers out to (and beyond) redshifts $z \gtrsim 10$ and measure the merger rate with percent-level precision (e.g., M. Punturo et al. 2010; D. Reitze et al. 2019; M. Maggiore et al. 2020; M. Evans et al. 2021, 2023; N. Singh et al. 2022; M. Branchesi et al. 2023; I. Gupta et al. 2023).

4.3. Caveats

The behavior of the redshift-dependent merger rate of BHNS, BNS, and BBH binaries is impacted by effects beyond those studied in the scope of the paper. We mention the most important ones here.

First, as mentioned in Section 4.1, formation channels beyond the isolated formation channel can impact the merger rate by contributing additional binaries. Each of these channels comes with their own unique uncertainties, increasing the complexity of understanding the overall merger rate behavior (e.g., M. Dominik et al. 2013; M. Zevin et al. 2021; G. Franciolini et al. 2022; I. Mandel & F. S. Broekgaarden 2022; M. Arca Sedda et al. 2023, and the references therein).

Second, not only the merger rate, but also the properties (i.e., masses, BH spins, and mass ratio) of the compact objects are redshift dependent as a result of both their birth environments depending on redshift (e.g., metallicity), as well as the varying range of merger delay times by a given z (e.g., M. Dominik et al. 2013; T. Kinugawa et al. 2020; M. Mapelli et al. 2022; B. McKernan et al. 2022; L. A. C. van Son et al. 2022a). Future work should further investigate the correlation between the merger rate and the properties of NSs and BHs in source binaries as a function of redshift to further aid in understanding the underlying physics and formation channels of mergers (e.g., Y. Qin et al. 2018; R. Abbott et al. 2021b; M. Fishbach et al.

[13] See https://observing.docs.ligo.org/plan/index.html for the most up-to-date information.

2021; S. S. Bavera et al. 2022a; K. Belczynski et al. 2022a; S. Biscoveanu et al. 2022; L. A. C. van Son et al. 2022a; T. A. Callister & W. M. Farr 2024).

Third, the underlying metallicity-dependent star formation history is uncertain, especially at higher redshift $z \gtrsim 4$ (see M. Chruslinska & G. Nelemans 2019; M. Chruślińska 2024, and the references therein). Although we expect the qualitative results in this study to be the same for different $\mathcal{S}(Z_i, z)$ models, the quantitative results (i.e., with what factor the merger rate deviates from an SFRD's redshift evolution) will likely depend on the choice of the metallicity-dependent star formation rate assumed. This is because $\mathcal{S}(Z_i, z)$ describes the number of systems formed at a given metallicity as a function of redshift, and will therefore govern when and how much the drop in BBH formation efficiency (Figure 3) will impact the merger rate distribution.

Fourth, there are many uncertainties in the physics underlying single and binary stellar evolution that can impact our study beyond the parameters considered here. A complete study is beyond the scope of this paper (and any single study), so we refer the interested reader to studies including F. Santoliquido et al. (2021), M. Mapelli (2021), F. S. Broekgaarden et al. (2022), I. Mandel & F. S. Broekgaarden (2022), K. Belczynski et al. (2022b), and M. Spera et al. (2022) and the references therein. The most important effects that can impact this study will be the uncertainties relating to the formation efficiency behavior (Figure 3) and/or that drastically alter the delay time distributions of BBH, BHNS, and BNS mergers. In particular, models with weak stellar wind loss have found a more gradual decrease in the BBH merger efficiency at high metallicity (e.g., F. S. Broekgaarden et al. 2022). For the delay time distributions, the angular momentum transport and mass transfer physics (and effects from radial expansion, e.g., E. Laplace et al. 2020; A. Romagnolo et al. 2023) are important uncertainties that impact the separation at which binaries form and thus the merger time. These should be the focus of future work (e.g., P. Agrawal et al. 2023; A. Dorozsmai & S. Toonen 2024).

5. Conclusions

In this paper we studied how the BBH merger rate expected from isolated binary evolution deviates from the cosmic SFRD, focusing on two key effects: metallicity-dependent formation rates and delay times. To achieve this, we conducted a grid of 4×3 simulations using the population synthesis code COMPAS, varying the CE efficiency and mass transfer efficiency parameters. We compared our simulated BBH rates to different SFRD-based models from the literature, and performed similar analysis with BHNS and BNS mergers from our simulations. Below, we summarize our main findings.

1. Simulated BBH merger rates can deviate significantly (factors up to 3.5–5) from a merger rate model described by a scaled SFRD (Figure 1 and Table 1).
2. These deviations are caused by simulations experiencing (i) more efficient formation of BBHs at low metallicity, leading to a shift of the BBH formation rate peak to $z \sim 2.5$ as opposed to $z \sim 2$ for the SFRD (Figures 2 and 3) and (ii) a broad distribution of delay times that create time gaps from formation to merger, boosting the merger rate at lower redshifts (Figure 4).
3. Many of our simulations display a redshift dependence in the BBH delay time distribution, favoring shorter delay times at higher redshifts (Figure 5). This is caused by a complex interplay between metallicity and formation channels causing more orbital shrinking for binaries formed at low metallicity and high redshift. We find that the CE efficiency parameter has a strong impact on this redshift evolution.
4. Our simulated BBH merger rates deviate from SFRD models convolved with delay times (Figure 6 and Table 1). This is because delayed SFRD models for the BBH rate fail to include the metallicity dependence of BBH formation found in our simulations, which causes a decrease in BBH formation at low z.
5. We find even larger deviations (up to factors $\sim$10) when comparing the simulated BBH merger rates to SFRD models scaled to the local merger rate, with the largest deviations at higher redshifts $z \gtrsim 3$ (Figure 7). This means studies that use SFRD-based merger rates that are matched to the local GW merger rate might under- or overestimate the underlying BBH merger rate by an order of magnitude at these higher redshifts. The high-z regime will be of particular relevance in coming years when the frontier of GW observations is pushed to the early years of our Universe.
6. Similarly to BBHs, we find that our simulated BHNS and BNS merger rates deviate from a scaled SFRD rate (Figures 8 and 9). We do find, however, that the simulated BHNS and BNS merger rates are more impacted by our our model's parameter prescriptions than for the BBHs.
7. Some of the simulated BHNS and BNS merger rates deviate from a simple SFRD-like redshift evolution parameterized by two slopes and a peak, and may actually include breaks before the peak (e.g., our $\alpha_{\rm CE} = 0.1$ models in Figure 9).

Overall, we find that the simulated BBH, BHNS, and BNS merger rates of the isolated binary evolution channel can significantly deviate from a scaled cosmic star formation rate. This motivates the use of non-SFRD-based merger rate models for future studies and exploration of the merger population.

Acknowledgments

A.P.B. acknowledges support from the Harvard PRISE and HCRP fellowships. F.S.B. acknowledges support for this work through the NASA FINESST scholarship 80NSSC22K1601 and from the Simons Foundation as part of the Simons Foundation Society of Fellows under award No. 1141468. F.S.B. also thanks the Steward Astronomy Department at the University of Arizona and the CCA at the Simons Foundation for providing a work place during this project.

Software: This paper made use of simulations from A. Boesky et al. (2024) which are publicly available at GW Landscape (http://gwlandscape.org.au/compas/). To create this data set, we used the COMPAS rapid binary population synthesis code version 2.31.04, which is available for free at http://github.com/TeamCOMPAS/COMPAS (Team COMPAS et al. 2022). The authors used STROOPWAFEL from F. S. Broekgaarden et al. (2019), publicly available at https://github.com/FloorBroekgaarden/STROOPWAFEL. The authors' primary programming language was PYTHON

from the Python Software Foundation available at http://www.python.org (G. van Rossum 1995). In addition, the following Python packages were used: MATPLOTLIB (J. D. Hunter 2007), NUMPY (C. R. Harris et al. 2020), SCIPY (P. Virtanen et al. 2020), IPYTHON/JUPYTER (F. Perez & B. E. Granger 2007; T. Kluyver et al. 2016), ASTROPY (T. A. Collaboration et al. 2018), and https://docs.h5py.org/en/stable/HDF5 (A. Collette 2013).

Appendix A
The Impact of Metallicity on Stellar Evolution

Metallicity plays a major role in both single and binary star evolution (C. J. Neijssel et al. 2019; F. S. Broekgaarden et al. 2022; M. Chruślińska 2024), predominantly as a direct result of its impact on stellar winds (J. S. Vink et al. 2001). Winds from massive stars are driven by spectral lines from metals. Wind strips mass from stars, so stars with a high initial metallicity lose significantly more mass in their lifetimes than metal-poor stars. This leads to stars born with greater proportions of metals to form NSs instead of BHs. The effects of metallicity on binary stellar evolution are numerous and even more complex than for single stars. Overall, stronger stellar winds at higher metallicity lead to a decrease in mergers of all types in our simulations due to a range of indirect effects including mass loss associated with stellar winds leading to a loss of angular momentum in the binary. This causes greater widening of binaries at high metallicities, increasing the inspiral times (P. C. Peters 1964) and the number of systems that disrupt, ultimately leading to a decrease in mergers from metal-rich progenitors. More mass loss through stellar winds also leads to systems with smaller stellar envelopes when the binary enters the CE phase. This also leads to less shrinking and fewer systems that can merge in a Hubble time (see C. J. Neijssel et al. 2019; F. S. Broekgaarden et al. 2022; M. Chruślińska 2024, and the references therein). Another important effect is that metallicity plays a considerable role in determining stellar radial expansion during the star's evolution with higher metallicities, typically leading to more radial expansion in our simulations (J. R. Hurley et al. 2000, 2002; A. Romagnolo et al. 2023), increasing the probability of unstable mass transfer and thus encouraging stellar mergers (e.g., C. J. Neijssel et al. 2019).

Appendix B
The Impact of the Metallicity-dependent Star Formation History

Throughout this work we have used a single model for the metallicity-dependent SFRD, but different star formation assumptions can impact the quantitative outcomes of our results. Figure 10 demonstrates this by showing the deviations of the redshift-dependent BBH merger rate from the assumed SFRD for our fiducial model as well as two other metallicity-specific SFRD models that span a large range of uncertainties in cosmic history (e.g., F. S. Broekgaarden et al. 2022).

Overall, we find that our main conclusions hold—the shape of the redshift-dependent BBH merger rate always deviates from that of the assumed SFRD because it is shifted to high z due to the boost in formation efficiency at low initial metallicity, but also shifted to low z due to the delay times between formation and merger. There are some differences compared to our fiducial metallicity-specific SFRD model. Specifically, the model that assumes the L. Strolger et al. (2004) SFRD, the M. Furlong et al. (2015) GSMF, and the X. Ma et al. (2016) MZR results in a merger rate with similar behavior to the fiducial model for $z \gtrsim 3$, but produces relatively fewer mergers at $z \lesssim 3$. As is shown in Figure 11, this is because it has a larger proportion of stars formed with low metallicity ($Z \lesssim Z_{\odot}/5$) at high redshifts. Due to the lower metallicities, the BBH merger rate is boosted until $z \gtrsim 2$–3, leading to a relatively low BBH merger deviation for $z \lesssim 2$.

A similar effect can also be seen in the metallicity-specific SFRD variation that assumes a P. Madau & T. Fragos (2017) SFRD, B. Panter et al. (2004) GSMF, and N. Langer & C. A. Norman (2006) MZR with offset—it also has a slightly

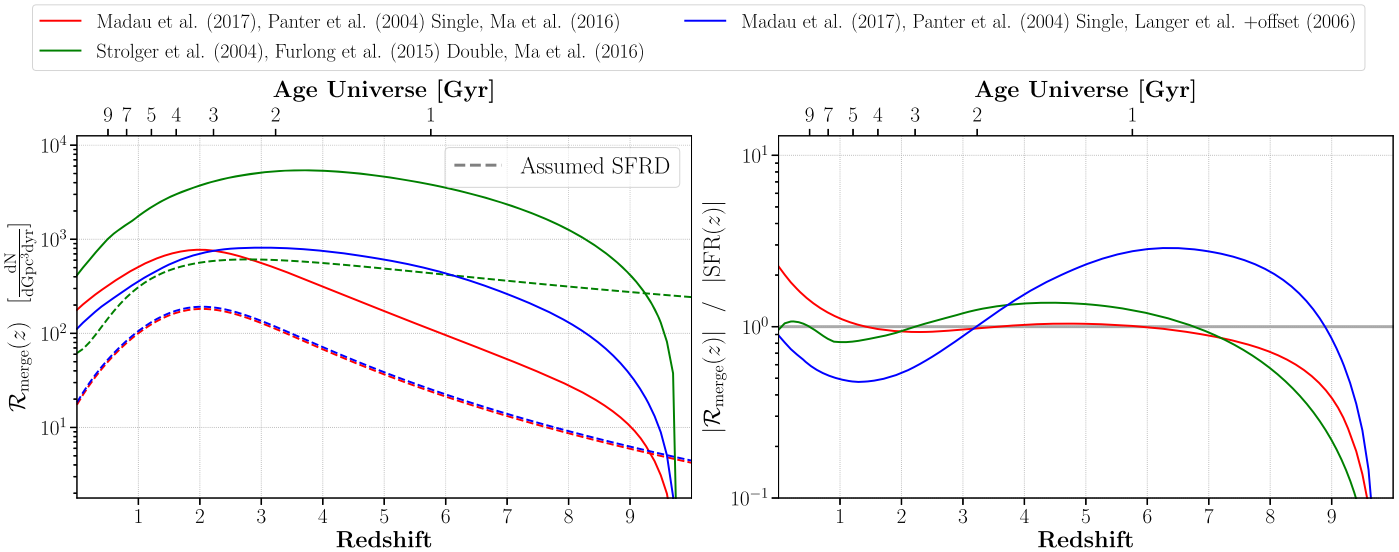

Figure 10. The same as Figure 1 except for variations in the metallicity-specific SFRD instead of binary physics. The panels show the fiducial metallicity-specific SFRD model (red), a variation assuming the L. Strolger et al. (2004) SFRD, the M. Furlong et al. (2015) GSMF, and the X. Ma et al. (2016) MZR (green), as well as a variation assuming a P. Madau & T. Fragos (2017) SFRD, the B. Panter et al. (2004) GSMF, and the N. Langer & C. A. Norman (2006) with an offset MZR.

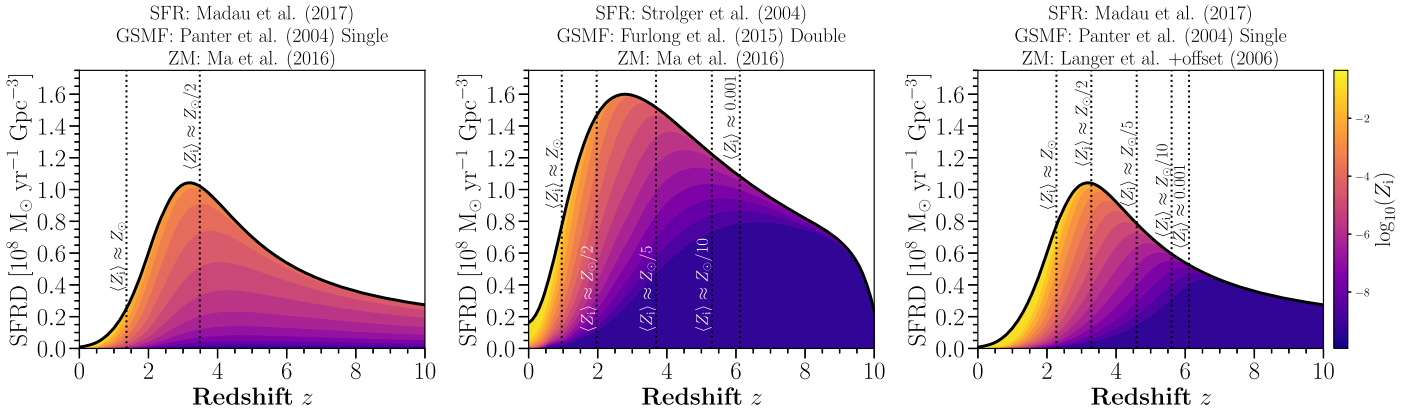

Figure 11. The assumed SFRD colored by the stars' initial metallicity, Z_i, for the different MSSFRs from Figure 10. The MSSFR labels are indicated above each panel, and the dotted lines show the redshift location of a few mean metallicities (i.e., the average metallicity of stars formed at a given redshift).

stronger contribution from low metallicity star formation compared to our fiducial model, but assumes the same SFRD (see Figure 11). We showed in Figure 2 that the formation yield of BBH mergers in our simulations drastically drops for stars formed with $Z_i \gtrsim Z_\odot/5$. This fact implies that metallicity effects therefore are causing the alternative metallicity-dependent SFRDs to produce fewer merging BBHs at redshifts $z \lesssim 3$.

Appendix C
The Shape of the Merger Rate Due to Different Delay Time Magnitudes

In Figure 12, we show how the delay times affect a synthetic distribution of stars throughout cosmic history. We rejection sample the SFRD from one million stars out to redshift 10, which we plot in black. We then age the sample stars by 10 Myr, 100 Myr, and 1 Gyr and plot their distributions. In the left panel, we see that the stars travel to lower redshift throughout their lifetimes; in other words, the distributions of the aged stars shift increasingly from the birth distribution toward lower redshift. Furthermore, this effect only causes a notable deviation from the star formation rate when the delay time is of order 500 Myr. A nontrivial aspect of this shift is the fact that the relationship between time and redshift is nonlinear. As we can see from the difference between the x-axes on the bottom and top of the panels, time passes faster at higher redshift. This implies that a star born at a high redshift should travel more redshift during its lifetime before merging than if it were born at low redshift.

In the right panel of Figure 12, we take the distributions from the left panel, normalize them, and then divide by the normalized assumed SFRD (similarly to the right panel of Figure 1). The horizontal gray line is what we would observe if the distribution of stars exactly followed the SFRD. Again, we observe that the longer stars are allowed to evolve, the lower redshift they travel to. The stars that were aged by 1 Gyr in particular show the extent to which the delay times can cause the distributions to shift to lower redshift, as the distribution is far above the SFRD (gray line) for redshifts lower than $z \sim 3$, and higher for redshifts above.

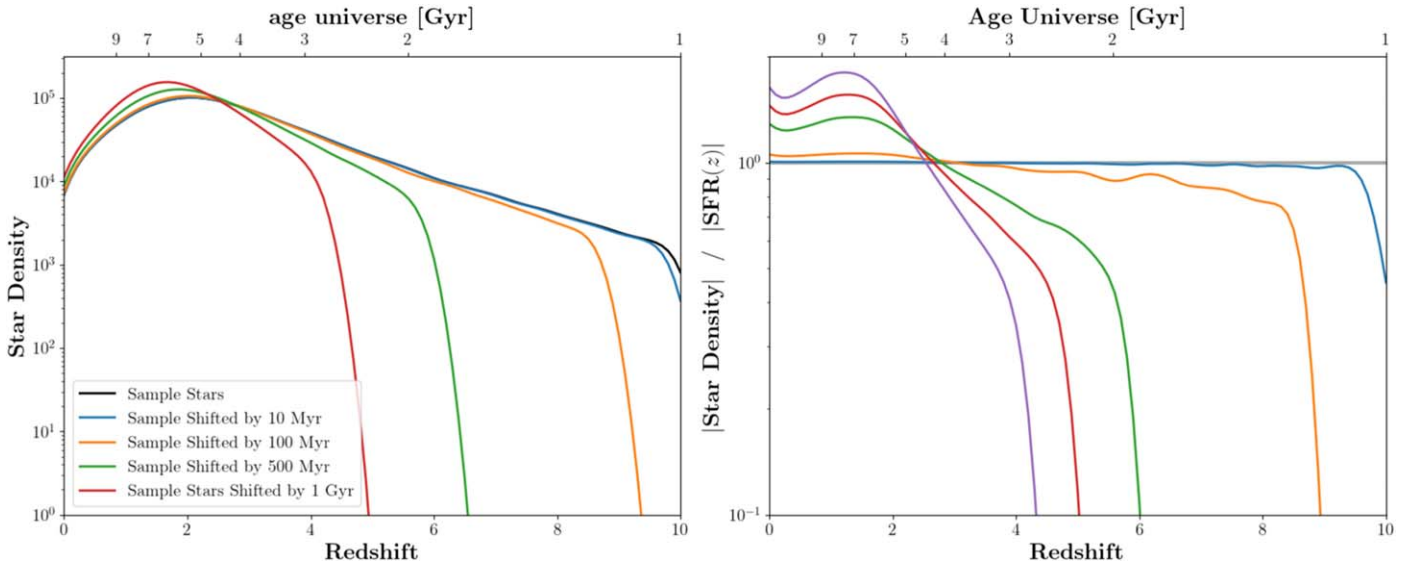

Figure 12. The effect of the delay time on the distribution of stars throughout cosmic history. We use rejection sampling of one million stars to acquire a sample of stars reflecting the assumed SFRD (P. Madau & T. Fragos 2017). Then, we add 10 Myr, 100 Myr, and 1 Gyr to their birth ages. The left panel shows the original distribution and the distributions of the stars shifted by the three different example delay times. In the right panel, we normalize each distribution and then divide by the normalized SFRD. In doing so, we can see how the delay time effects cause the population of stars at low redshift to be greater than the SFRD.

Appendix D
Binary Black Hole Formation Channels as a Function of Redshift

As was discussed in the main body of this paper, the delay time distribution is strongly correlated with the formation channels that lead to mergers. In Figure 13, we show the percentage contribution of the main formation channels as described in F. S. Broekgaarden et al. (2021) to the merger rate as a function of redshift for all models in grid A. Clearly, the formation pathways that BBH merger progenitors follow are highly dependent on the physical assumptions—the contributions of each formation channel to the merger rate are vastly different from model to model. Furthermore, the proportion of mergers created by each channel changes considerably throughout cosmic history, again likely as a result of the difference in the initial metallicity of the BBHs progenitors at different redshifts and their interplay with the model prescriptions. Noticeably, the trends in channel contribution also appears to be similar for each group of models with the same assumed $\alpha_{\rm CE}$. This observation is the cause of the delay time distributions being grouped by $\alpha_{\rm CE}$—the shape of the median delay times throughout cosmic history are similar because the proportion of mergers created by each channel is the same. Furthermore, the models with $\alpha_{\rm CE} = 2.0$, which have the most distinct median delay time shape, have a drastic increase in the proportion of mergers formed through the classic channel (with a CE phase), which corresponds to a drastic decrease in the median delay time from $z = 0$ to $z \approx 3$ as at higher redshift the BBH systems form through the classic CE channel, which leads to shorter delay times compared to the only stable mass transfer channel. This is in agreement with studies such as A. Olejak et al. (2022) and L. A. C. van Son et al. (2022b) who found that channels that include CEs tend to have lower delay times. Ultimately, the most important conclusion from this figure is that the delay time distribution is strongly dependent on the channels that the BBH mergers follow, and changes in the channel contributions throughout cosmic history are highly nontrivial and dependent on the model assumptions.

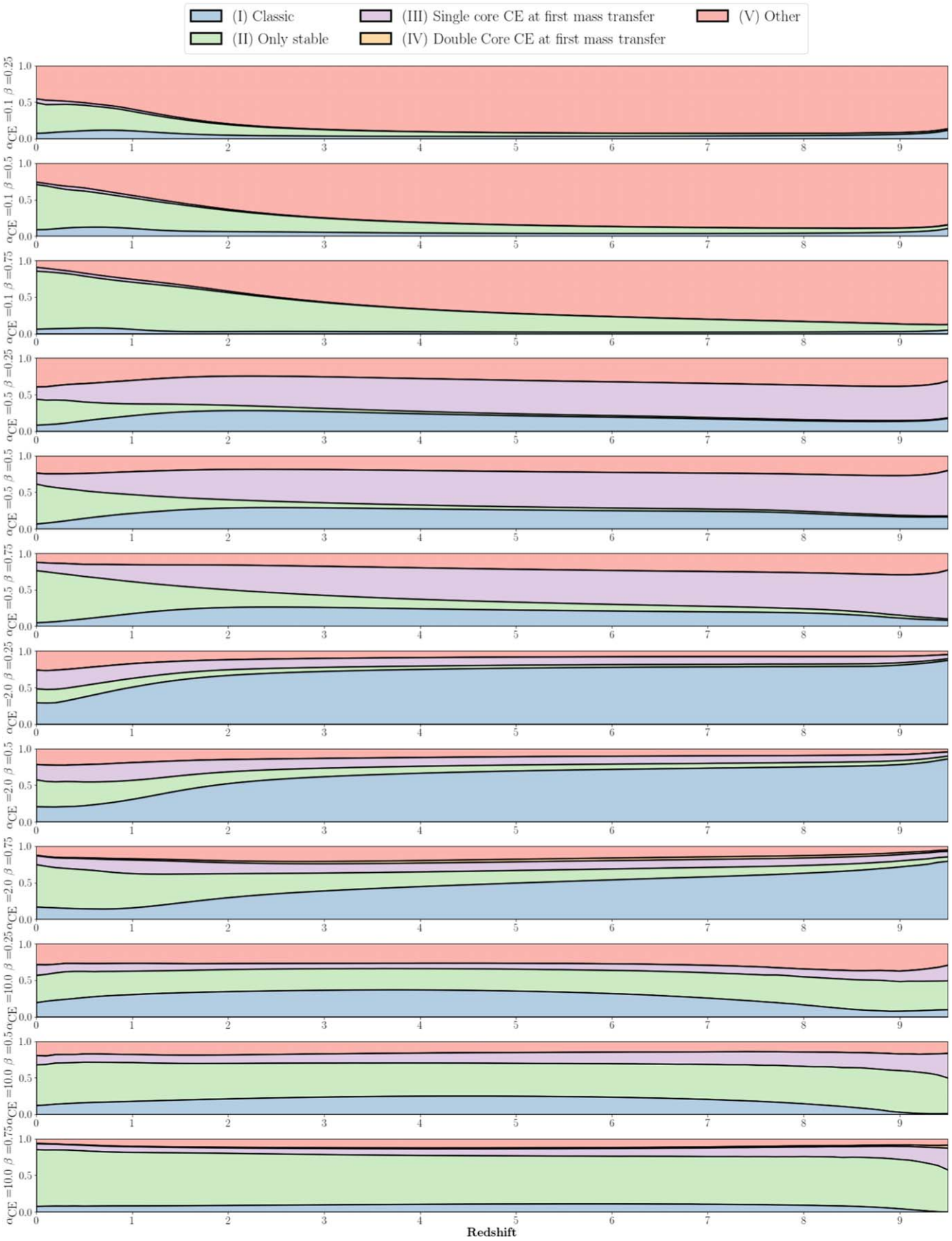

Figure 13. The percentage contributions of each formation channel (as described in F. S. Broekgaarden et al. 2021) for the merger rates as a function of redshift of all models in grid A.

Appendix E
Deviations between the Simulations and Toy Models

Table 1 shows the deviations at different redshifts between our simulated merger rates and the toy model merger rates.

Table 1
The Minimum, Maximum, and Median of the Normalized Binary Black Hole Merger Rates for Each Model Divided by Normalized Delayed Variations of the Star Formation Rate Density for Redshift Values 0–9

	No Delay			$t_{\rm delay} \propto \delta(t - 20\ {\rm Myr})$			$t_{\rm delay} \propto 1/t$		
Redshift	Minimum	Median	Maximum	Minimum	Median	Maximum	Minimum	Median	Maximum
$z = 0$	1.27	2.43	3.48	1.74	3.33	4.76	0.21	0.41	0.59
$z = 1$	0.94	1.26	1.62	0.90	1.22	1.56	0.59	0.80	1.02
$z = 2$	0.90	0.95	1.00	0.89	0.94	0.98	1.07	1.13	1.18
$z = 3$	0.79	0.90	1.02	0.78	0.89	1.00	0.97	1.11	1.26
$z = 4$	0.73	0.97	1.10	0.72	0.95	1.09	0.89	1.18	1.35
$z = 5$	0.67	0.99	1.12	0.68	1.01	1.15	0.94	1.39	1.58
$z = 6$	0.59	0.96	1.10	0.63	1.02	1.16	1.03	1.67	1.90
$z = 7$	0.49	0.87	1.01	0.56	0.99	1.16	1.10	1.94	2.26
$z = 8$	0.37	0.70	0.86	0.46	0.88	1.08	1.12	2.16	2.63
$z = 9$	0.20	0.41	0.59	0.30	0.61	0.89	1.03	2.07	3.00

Note. The first three columns use a toy model rate by rescaling an SFRD with no delay, the middle three columns use as a toy model an SFRD with a constant delay of 20 Myr, and the last three columns use for the toy model a scaled SFRD with a delay time distribution using t^{-1} with $\min(t_{\rm delay}) = 20$ Myr.

ORCID iDs

Adam P. Boesky https://orcid.org/0009-0005-9830-9966
Floor S. Broekgaarden https://orcid.org/0000-0002-4421-4962
Edo Berger https://orcid.org/0000-0002-9392-9681

References

Abbott, B. P., Abbott, R., Abbott, T. D., et al. 2018, LRR, 21, 3
Abbott, B. P., Abbott, R., Abbott, T. D., et al. 2019, PhRvX, 9, 031040
Abbott, R., Abbott, T. D., Abraham, S., et al. 2021a, PhRvX, 11, 021053
Abbott, R., Abbott, T. D., Abraham, S., et al. 2021b, ApJL, 913, L7
Abbott, R., Abbott, T. D., Acernese, F., et al. 2023a, PhRvX, 13, 041039
Abbott, R., Abbott, T. D., Acernese, F., et al. 2023b, PhRvX, 13, 011048
Abbott, R., Abbott, T. D., Acernese, F., et al. 2024, PhRvD, 109, 022001
Agrawal, P., Hurley, J., Stevenson, S., et al. 2023, MNRAS, 525, 933
Arca Sedda, M., Naoz, S., & Kocsis, B. 2023, Univ, 9, 138
Bavera, S. S., Fishbach, M., Zevin, M., Zapartas, E., & Fragos, T. 2022a, A&A, 665, A59
Bavera, S. S., Fragos, T., Zevin, M., et al. 2021, A&A, 647, A153
Bavera, S. S., Franciolini, G., Cusin, G., et al. 2022b, A&A, 660, A26
Belczynski, K., Bulik, T., Olejak, A., et al. 2018, arXiv:1812.10065
Belczynski, K., Doctor, Z., Zevin, M., et al. 2022a, ApJ, 935, 126
Belczynski, K., Holz, D. E., Bulik, T., & O'Shaughnessy, R. 2016, Natur, 534, 512
Belczynski, K., Romagnolo, A., Olejak, A., et al. 2022b, ApJ, 925, 69
Belczynski, K., Ryu, T., Perna, R., et al. 2017, MNRAS, 471, 4702
Belgacem, E., Dirian, Y., Foffa, S., et al. 2019, JCAP, 2019, 015
Berger, E. 2014, ARA&A, 52, 43
Biscoveanu, S., Callister, T. A., Haster, C.-J., et al. 2022, ApJL, 932, L19
Boesky, A., Broekgaarden, F. S., & Berger, E. 2024, ApJ, in press, arXiv:2405.01630
Borhanian, S., & Sathyaprakash, B. S. 2024, PhRvD, 110, 083040
Branchesi, M., Maggiore, M., Alonso, D., et al. 2023, JCAP, 2023, 068
Broekgaarden, F. S., Berger, E., Neijssel, C. J., et al. 2021, MNRAS, 508, 5028
Broekgaarden, F. S., Berger, E., Stevenson, S., et al. 2022, MNRAS, 516, 5737
Broekgaarden, F. S., Justham, S., de Mink, S. E., et al. 2019, MNRAS, 490, 5228
Callister, T. A., & Farr, W. M. 2024, PhRvX, 14, 021005
Cheng, A. Q., Zevin, M., & Vitale, S. 2023, ApJ, 955, 127
Choksi, N., Volonteri, M., Colpi, M., Gnedin, O. Y., & Li, H. 2019, ApJ, 873, 100
Chruslinska, M., & Nelemans, G. 2019, MNRAS, 488, 5300
Chruslinska, M., Nelemans, G., & Belczynski, K. 2018, MNRAS, 482, 5012
Chruślińska, M. 2024, AnP, 536, 2200170
Chu, Q., Yu, S., & Lu, Y. 2022, MNRAS, 509, 1557
Collaboration, T. A., Price-Whelan, A. M., Sipőcz, B. M., et al. 2018, AJ, 156, 123
Collette, A. 2013, Python and HDF5 (Sebastopol, CA: O'Reilly)
Colombo, A., Salafia, O. S., Gabrielli, F., et al. 2022, ApJ, 937, 79
de Kool, M. 1990, ApJ, 358, 189
De Luca, V., Desjacques, V., Franciolini, G., & Riotto, A. 2020, JCAP, 2020, 028
De Luca, V., Franciolini, G., Pani, P., & Riotto, A. 2021, JCAP, 2021, 039
de Mink, S. E., & Mandel, I. 2016, MNRAS, 460, 3545
Dominik, M., Belczynski, K., Fryer, C., et al. 2013, ApJ, 779, 72
Dorozsmai, A., & Toonen, S. 2024, MNRAS, 530, 3706
du Buisson, L., Marchant, P., Podsiadlowski, P., et al. 2020, MNRAS, 499, 5941
Edelman, B., Farr, B., Doctor, Z., et al. 2023, ApJ, 946, 16
Eggleton, P. P., Fitchett, M. J., & Tout, C. A. 1989, ApJ, 347, 998
Eldridge, J. J., Stanway, E. R., & Tang, P. N. 2019, MNRAS, 482, 870
Evans, M., Adhikari, R. X., Afle, C., et al. 2021, arXiv:2109.09882
Evans, M., Corsi, A., Afle, C., et al. 2023, arXiv:2306.13745
Fishbach, M., Doctor, Z., Callister, T., et al. 2021, ApJ, 912, 98
Fishbach, M., Holz, D. E., & Farr, W. M. 2018, ApJL, 863, L41
Fishbach, M., Kimball, C., & Kalogera, V. 2022, ApJL, 935, L26
Fong, W., Berger, E., Margutti, R., & Zauderer, B. A. 2015, ApJ, 815, 102
Fragione, G., & Kocsis, B. 2018, PhRvL, 121, 161103
Franciolini, G., Cotesta, R., Loutrel, N., et al. 2022, PhRvD, 105, 063510
Furlong, M., Bower, R. G., Theuns, T., et al. 2015, MNRAS, 450, 4486
Giacobbo, N., & Mapelli, M. 2018, MNRAS, 480, 2011
Giacobbo, N., Mapelli, M., & Spera, M. 2018, MNRAS, 474, 2959
Godfrey, J., Edelman, B., & Farr, B. 2023, arXiv:2304.01288
Gupta, I., Afle, C., Arun, K. G., et al. 2023, arXiv:2307.10421

Harris, C. R., Millman, K. J., van der Walt, S. J., et al. 2020, Natur, 585, 357
Hijikawa, K., Tanikawa, A., Kinugawa, T., Yoshida, T., & Umeda, H. 2021, MNRAS, 505, L69
Hunter, J. D. 2007, CSE, 9, 90
Hurley, J. R., Pols, O. R., & Tout, C. A. 2000, MNRAS, 315, 543
Hurley, J. R., Tout, C. A., & Pols, O. R. 2002, MNRAS, 329, 897
Iacovelli, F., Mancarella, M., Foffa, S., & Maggiore, M. 2022, ApJ, 941, 208
Ivanova, N., Justham, S., & Ricker, P. 2020, Common Envelope Evolution (Bristol: IOP Publishing)
Kinugawa, T., Inayoshi, K., Hotokezaka, K., Nakauchi, D., & Nakamura, T. 2014, MNRAS, 442, 2963
Kinugawa, T., Nakamura, T., & Nakano, H. 2020, MNRAS, 498, 3946
Kippenhahn, R., & Weigert, A. 1990, Stellar Structure and Evolution (Berlin: Springer)
Klencki, J., Moe, M., Gladysz, W., et al. 2018, A&A, 619, A77
Kluyver, T., Ragan-Kelley, B., Pérez, F., et al. 2016, Jupyter Notebooks – a Publishing Format for Reproducible Computational Workflows (Amsterdam: IOS Press), 87
Kritos, K., Strokov, V., Baibhav, V., & Berti, E. 2024, PhRvD, 110, 043023
Kruckow, M. U., Tauris, T. M., Langer, N., Kramer, M., & Izzard, R. G. 2018, MNRAS, 481, 1908
Langer, N. 2012, ARA&A, 50, 107
Langer, N., & Norman, C. A. 2006, ApJ, 638, L63
Laplace, E., Götberg, Y., de Mink, S. E., Justham, S., & Farmer, R. 2020, A&A, 637, A6
Lehoucq, L., Dvorkin, I., Srinivasan, R., Pellouin, C., & Lamberts, A. 2023, MNRAS, 526, 4378
Lipunov, V. M., Kornilov, V., Gorbovskoy, E., et al. 2017, NewA, 51, 122
Liu, B., & Bromm, V. 2021, MNRAS, 506, 5451
Ma, X., Hopkins, P. F., Faucher-Giguère, C.-A., et al. 2016, MNRAS, 456, 2140
Madau, P., & Dickinson, M. 2014, ARA&A, 52, 415
Madau, P., & Fragos, T. 2017, ApJ, 840, 39
Maggiore, M., Van Den Broeck, C., Bartolo, N., et al. 2020, JCAP, 2020, 050
Mandel, I., & Broekgaarden, F. S. 2022, LRR, 25, 1
Mandel, I., & de Mink, S. E. 2016, MNRAS, 458, 2634
Mapelli, M. 2021, Handbook of Gravitational Wave Astronomy (Berlin: Springer), 16
Mapelli, M., Bouffanais, Y., Santoliquido, F., Arca Sedda, M., & Artale, M. C. 2022, MNRAS, 511, 5797
Martinez, M. A. S., Fragione, G., Kremer, K., et al. 2020, ApJ, 903, 67
McKernan, B., Ford, K. E. S., Callister, T., et al. 2022, MNRAS, 514, 3886
Mehta, A. K., Olsen, S., Wadekar, D., et al. 2023, arXiv:2311.06061
Mennekens, N., & Vanbeveren, D. 2016, A&A, 589, A64
Naidu, R. P., Ji, A. P., Conroy, C., et al. 2022, ApJL, 926, L36
Neijssel, C. J., Vigna-Gomez, A., Stevenson, S., et al. 2019, MNRAS, 490, 3740
Ng, K. K. Y., Vitale, S., Farr, W. M., & Rodriguez, C. L. 2021, ApJL, 913, L5
Nitz, A. H., Kumar, S., Wang, Y.-F., et al. 2023, ApJ, 946, 59
Nugent, A. E., Fong, W.-F., Dong, Y., et al. 2022, ApJ, 940, 57
Olejak, A., Fryer, C. L., Belczynski, K., & Baibhav, V. 2022, MNRAS, 516, 2252
Olejak, A., Klencki, J., Xu, X.-T., et al. 2024, A&A, 689, A305
Olsen, S., Venumadhav, T., Mushkin, J., et al. 2022, PhRvD, 106, 043009
Panter, B., Heavens, A. F., & Jimenez, R. 2004, MNRAS, 355, 764
Payne, E., & Thrane, E. 2023, PhRvR, 5, 023013
Perez, F., & Granger, B. E. 2007, CSE, 9, 21
Peters, P. C. 1964, PhRv, 136, B1224
Pols, O. R., Schroder, K.-P., Hurley, J. R., Tout, C. A., & Eggleton, P. P. 1998, MNRAS, 298, 525
Punturo, M., Abernathy, M., Acernese, F., et al. 2010, CQGra, 27, 194002
Qin, Y., Fragos, T., Meynet, G., et al. 2018, A&A, 616, A28
Raidal, M., Spethmann, C., Vaskonen, V., & Veermäe, H. 2019, JCAP, 2019, 018
Ray, A., Hernandez, I. M., Mohite, S., Creighton, J., & Kapadia, S. 2023, ApJ, 957, 37
Regimbau, T., Dent, T., Del Pozzo, W., et al. 2012, PhRvD, 86, 122001
Reitze, D., Adhikari, R. X., Ballmer, S., et al. 2019, BAAS, 51, 35
Riley, J., Mandel, I., Marchant, P., et al. 2021, MNRAS, 505, 663
Rodriguez, C. L., Chatterjee, S., & Rasio, F. A. 2016, PhRvD, 93, 084029
Rodriguez, C. L., & Loeb, A. 2018, ApJL, 866, L5
Romagnolo, A., Belczynski, K., Klencki, J., et al. 2023, MNRAS, 525, 706
Román-Garza, J., Bavera, S. S., Fragos, T., et al. 2021, ApJL, 912, L23
Santoliquido, F., Mapelli, M., Giacobbo, N., Bouffanais, Y., & Artale, M. C. 2021, MNRAS, 502, 4877
Santoliquido, F., Mapelli, M., Iorio, G., et al. 2023, MNRAS, 524, 307
Singh, N., Bulik, T., Belczynski, K., & Askar, A. 2022, A&A, 667, A2
Spera, M., Trani, A. A., & Mencagli, M. 2022, Galax, 10, 76
Stevenson, S., Vigna-Gomez, A., Mandel, I., et al. 2017, NatCo, 8, 14906
Strolger, L.-G., Riess, A. G., Dahlen, T., et al. 2004, ApJ, 613, 200
Team COMPAS, Riley, J., Agrawal, P., et al. 2022, ApJS, 258, 34
Tong, H., Galaudage, S., & Thrane, E. 2022, PhRvD, 106, 103019
Tout, C. A., Pols, O. R., Eggleton, P. P., & Han, Z. 1996, MNRAS, 281, 257
van Rossum, G. 1995, Python tutorial, Tech. Rep. CS-R9526, Centrum voor Wiskunde en Informatica (CWI), Amsterdam
van Son, L. A. C., de Mink, S. E., Callister, T., et al. 2022a, ApJ, 931, 17
van Son, L. A. C., de Mink, S. E., Renzo, M., et al. 2022b, ApJ, 940, 184
Venumadhav, T., Zackay, B., Roulet, J., Dai, L., & Zaldarriaga, M. 2019, PhRvD, 100, 023011
Venumadhav, T., Zackay, B., Roulet, J., Dai, L., & Zaldarriaga, M. 2020, PhRvD, 101, 083030
Vigna-Gomez, A., Neijssel, C. J., Stevenson, S., et al. 2018, MNRAS, 481, 4009
Vijaykumar, A., Fishbach, M., Adhikari, S., & Holz, D. E. 2024, ApJ, 972, 157
Vink, J. S., de Koter, A., & Lamers, H. J. G. L. M. 2000, A&A, 362, 295
Vink, J. S., de Koter, A., & Lamers, H. J. G. L. M. 2001, A&A, 369, 574
Virtanen, P., Gommers, R., Oliphant, T. E., et al. 2020, NatMe, 17, 261
Vitale, S., Farr, W. M., Ng, K. K. Y., & Rodriguez, C. L. 2019, ApJL, 886, L1
Wadekar, D., Roulet, J., Venumadhav, T., et al. 2023, arXiv:2312.06631
Webbink, R. F. 1984, ApJ, 277, 355
Ye, C. S., & Fishbach, M. 2024, ApJ, 967, 62
Zackay, B., Venumadhav, T., Dai, L., Roulet, J., & Zaldarriaga, M. 2019, PhRvD, 100, 023007
Zevin, M., Bavera, S. S., Berry, C. P. L., et al. 2021, ApJ, 910, 152
Zevin, M., Nugent, A. E., Adhikari, S., et al. 2022, ApJL, 940, L18